arXiv:2511.16870v3 [cs.CV] 25 May 2026

Align & Invert: Solving Inverse Problems with Diffusion and Flow-based Models via Representation Alignment

Loukas Sfountouris
Department of Computer Science
University of Warwick
Coventry, England
loukas.sfountouris@warwick.ac.uk

Giannis Daras
Massachusetts Institute of Technology
Massachusetts, USA
gdaras@mit.edu

Paris Giampouras
Department of Computer Science
University of Warwick
Coventry, England
paris.giampouras@warwick.ac.uk

Abstract

Enforcing alignment between the internal representations of diffusion or flow-based generative models and those of pretrained self-supervised encoders has recently been shown to provide a powerful inductive bias, improving both convergence and sample quality. In this work, we extend this idea to inverse problems, where pretrained generative models are employed as *priors*. We propose applying *representation alignment* (REPA) between diffusion or flow-based models and a DINOv2 visual encoder, to guide the reconstruction process at inference time. Although ground-truth signals are unavailable in inverse problems, we show that aligning model representations of approximate target features can substantially enhance reconstruction quality and perceptual realism. We provide theoretical results showing (a) that REPA regularization can be viewed as a variational approach for minimizing a divergence measure in the DINOv2 space, and (b) how under certain regularity assumptions REPA updates steer the latent diffusion states toward those of the clean image. We integrate REPA into multiple state-of-the-art inverse problem solvers, and provide extensive experiments confirming that our method consistently improves reconstruction quality, while also reducing the number of discretization steps required to reach the same performance level as the underlying solver. Our code is publicly available at https://github.com/Sfountouris/Align_And_Invert.

1 Introduction

Pretrained diffusion and flow-based models, [31, 12, 20], have recently been at the heart of methods focusing on addressing various types of inverse problems. The crux of these approaches is to perform diffusion sampling, incorporating measurement information during the reverse process, with the goal to reconstruct the clean image at the final step, [24, 5, 34]. Undoubtedly, diffusion and flow-based models have pushed the boundaries in addressing a wealth of inverse problems, [6]. However, they still struggle to produce highly detailed images particularly in cases of severe degradation and in challenging scenes, such as natural images with rich textures and complex backgrounds. These issues are further exacerbated when using latent diffusion models [27], where the inclusion of encoder-

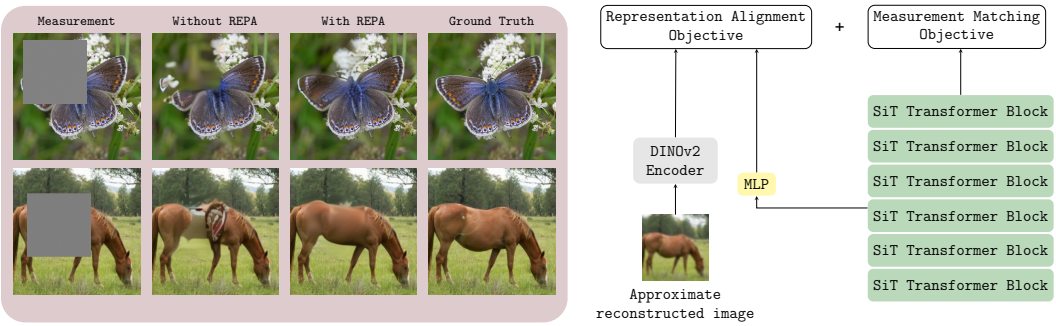


Figure 1: Overview of our proposed framework. Left: Box inpainting results, where adding REPA improves perceptual quality. Right: Alignment between diffusion features and DINOv2 embeddings.

decoder architectures introduces additional challenges during the reverse process due to nonlinearities. To mitigate these limitations, further inductive biases are needed during inference, [28, 26].

Recent studies have shown that diffusion models learn semantic features in their hidden states, [18]. The more expressive these features are the better the diffusion model performs on the generative task, [39]. Building on this insight, the seminal work of [42] introduced a regularizer that aligns the internal representations of the diffusion model with those of a pretrained visual encoder, [22]. This framework, termed *representation alignment* (REPA), was shown to act as a strong semantic constraint leading to higher-fidelity generations and significantly faster convergence.

The success of REPA has attracted considerable interest in this direction, [38, 35, 41, 17, 36]. In particular, [38] observed that while REPA enhances early training dynamics, its benefits diminish over time and can even degrade performance in later iterations. To address this issue, they introduced an early-stopping strategy which mitigated the late-stage degradation and further improved overall convergence speed. Other works have explored applying alignment losses directly to VAE latent spaces [41, 40], finding that diffusion models trained on these regularized spaces converge faster. Despite these advances, most efforts focus on improving training efficiency, whereas relatively little attention has been paid to leveraging representation alignment at inference time, particularly for solving inverse problems. This motivates our central question:

Can we apply representation alignment to benefit existing algorithms for solving inverse problems using pretrained diffusion and flow-based models?

Contributions. Our main contributions are as follows:

- We introduce a general framework for solving inverse problems with diffusion and flow-based models by enforcing alignment between internal diffusion representations and DINOv2 features (Fig. 1). Despite the absence of ground truth, alignment with proxy reconstructions remains effective thanks to the robustness/invariances of DINOv2 representations.
- We provide theoretical results that characterize the effect of the REPA regularizer: (a) its connection to a divergence measure defined in the DINOv2 feature space, and (b) under suitable regularity assumptions, its ability to steer latent diffusion states toward those associated with the clean image.
- We demonstrate the versatility of our approach by integrating representational alignment into different existing state-of-the-art inverse problem solvers.
- Through extensive experiments on super-resolution, Gaussian deblurring, motion deblurring, and box inpainting, we show consistent improvements over prior methods across tasks and metrics, and further demonstrate that applying REPA to existing solvers allows them to match their original performance using significantly fewer discretization steps.

2 Related Work

2.1 Diffusion & Flow-based Models

Generative models based on denoising are a class of deep generative models that aim to learn a data distribution $p_0(x)$ by training on progressively corrupted versions of real samples [31, 12, 33,

21]. These models define a) a forward (noising) process, which gradually interpolates between the data distribution and a reference distribution $p_1(x)$ (typically a Gaussian), and b) a reverse (denoising) process, which is trained to invert this corruption and iteratively reconstruct data from noise. Following the formulation of stochastic interpolants [1], the time marginals of this process can be expressed as

$$x_t = \alpha_t x^* + \sigma_t \varepsilon, \qquad x^* \sim p_0(x),\ \varepsilon \sim \mathcal{N}(0, I), \tag{1}$$

where α_t and σ_t correspond to decreasing and increasing functions of t, respectively, with boundary conditions $\alpha_0 = \sigma_1 = 1$ and $\alpha_1 = \sigma_0 = 0$. Throughout, we use the notation $\dot{\alpha}_t := \frac{\mathrm{d}\alpha_t}{\mathrm{d}t}$ and $\dot{\sigma}_t := \frac{\mathrm{d}\sigma_t}{\mathrm{d}t}$ to denote time derivatives. It was shown in [20] that there exists a probability flow ODE, $\dot{x}_t = v(x_t, t)$, whose solution follows the same time marginals as the process in eq. (1), where $v(x_t, t)$ denotes the true drift field transporting $p_0(x)$ to $p_1(x)$.

To enable sampling from the data distribution, one has to train a neural network $v_\theta(x_t, t)$ to approximate $v(x_t, t)$. This is done by regressing the network output toward the optimal vector field using *conditional flow matching* [20, 14], minimizing

$$\mathcal{L}_{\text{velocity}}(\theta) := \mathbb{E}_{x^*, \varepsilon, t}\left[\|v_\theta(x_t, t) - \dot{\alpha}_t x^* - \dot{\sigma}_t \varepsilon\|^2\right], \tag{2}$$

Beyond the ODE view, there also exists a reverse *stochastic differential equation* (SDE) with the same time marginals:

$$\mathrm{d}x_t = v(x_t, t)\,\mathrm{d}t - g^2(t)\, s(x_t, t)\,\mathrm{d}t + g(t)\,\mathrm{d}\bar{w}_t, \tag{3}$$

where $s(x_t, t) = \nabla_{x_t} \log p_t(x_t)$ is the score, $g(t)$ is the diffusion coefficient, and $\bar{w}_t$ is a standard Wiener process running backward in time. Notably, the score can be expressed directly in terms of the velocity field:

$$s(x_t, t) = \sigma_t^{-1} \cdot \frac{\alpha_t v(x_t, t) - \dot{\alpha}_t x_t}{\dot{\alpha}_t \sigma_t - \alpha_t \dot{\sigma}_t}. \tag{4}$$

Eq. (4) hints that the score parameterization used in diffusion models and the velocity parameterization used in flow-based models can lead to equivalent formulations of the sampling process. In practice, diffusion models correspond to a stochastic discretization of the probability flow ODE, while flow-based models correspond to its deterministic counterpart [16].

2.2 Diffusion Models with Representation Guidance

Diffusion models learn rich, discriminative features in their hidden states, which are crucial for their generative performance [39]. Nevertheless, their learned representations still fall behind on downstream tasks when compared with state-of-the-art self-supervised visual encoders, [3, 30]. This representation gap has been identified as a key bottleneck for improving the generative performance of diffusion models, as richer and more semantically structured representations have been shown to enhance sample fidelity [42]. To address this, a growing line of work introduces representation guidance, which conditions diffusion models on external representations from pretrained self-supervised encoders [19]. Typically these approaches fall into two categories: (i) conditioning the diffusion model on external representations, either learned, [19], or retrieved from a database of samples, [4, 13, 29]; and (ii) explicitly aligning the model's internal representations with those of large pretrained encoders, thereby encouraging more semantically meaningful feature-spaces, [35, 13, 17].

Within the REPA framework, feature-level alignment is applied directly to intermediate representations of the diffusion model. In particular, let the diffusion model consist of L transformer blocks, and $\ell \in \{1, \ldots, L\}$ denote the layer at which features are extracted. The quantity $h_t \in \mathbb{R}^{N \times D_2}$ denotes the matrix of patch tokens obtained after the first ℓ transformer blocks when the model processes an input image x at timestep t. Here, N is the number of patch tokens and D_2 the embedding dimension, with $h_t^{[n]} \in \mathbb{R}^{D_2}$ representing the n-th patch token. For convenience, this is written as $h_t = \text{DIFFENC}(x_t, t)$, where x_t denotes the noisy image and DIFFENC returns the patch-level hidden representation after the first ℓ blocks of the diffusion model's transformer encoder. REPA enforces patch-wise similarity between the D_1-dimensional DINOv2 representation of the target image x, i.e., $f_{\text{DINOv2}}^{[n]}(x) \in \mathbb{R}^{D_1}$ for patches $n = 1, \ldots, N$, and the intermediate hidden states $h_t^{[n]}$, by maximizing the following objective during training:

$$\text{REPA}(x, h_t) = \frac{1}{N} \sum_{n=1}^{N} \cos\Big(f_{\text{DINOv2}}^{[n]}(x),\ g_\phi\big(h_t^{[n]}\big)\Big), \tag{5}$$

where $g_\phi : \mathbb{R}^{D_2} \to \mathbb{R}^{D_1}$ is a learnable multi-layer perceptron (MLP) that projects hidden states into the DINOv2 space. By jointly optimizing $\mathcal{L}_{\text{REPA}}$ with the standard diffusion loss, the model learns internal representations that are semantically richer and better aligned with high-level visual features, ultimately yielding higher-quality image generation and faster convergence during training.

2.3 Inverse Problems with Diffusion and Flow Models

When solving inverse problems the goal is to recover the clean signal x_0 from noisy or degraded measurements y. In the flow- and diffusion-based framework, this is accomplished by replacing the unconditional score function in eq. (3) with the conditional score $\nabla_{x_t} \log p(x_t \mid y)$. Applying Bayes' rule, the conditional score can be decomposed as

$$\nabla_{x_t} \log p(x_t \mid y) = \nabla_{x_t} \log p_t(x_t) + \nabla_{x_t} \log p(y \mid x_t),$$

Using this decomposition, the reverse-time SDE becomes

$$dx_t = \big(v(x_t, t) - g^2(t)\, \nabla_{x_t} \log p(x_t \mid y)\big)\, dt + g(t)\, d\bar{w}_t.$$

The unconditional score $\nabla_{x_t} \log p_t(x_t)$ is provided by a pretrained diffusion or flow-based model, while the likelihood term $\nabla_{x_t} \log p(y \mid x_t)$ enforces measurement consistency but is generally intractable, as it requires marginalizing over all possible clean signals x_0. One of the most prominent approaches is *Diffusion Posterior Sampling (DPS)*, [5], which uses the following approximation:

$$p(y \mid x_t) \approx p\left(y \mid \hat{x}_0 = \mathbb{E}[x_0 \mid x_t]\right),$$

where $\mathbb{E}[x_0 \mid x_t]$ denotes the conditional expectation of x_0 given x_t. In many practical scenarios, performing the diffusion process directly in pixel space is computationally prohibitive. Latent diffusion models (LDMs) address this limitation by operating in a compressed latent space. Let $\mathcal{E} : \mathbb{R}^k \to \mathbb{R}^d$ be an encoder mapping an image x_0 to its latent representation $z_0 = \mathcal{E}(x_0)$, and let $\mathcal{D}$ denote the corresponding decoder such that $\hat{x}_0 = \mathcal{D}(z_0) \approx x_0$. Building on this formulation, recent work has proposed latent-space counterparts of pixel-based inverse problem solvers. For example, DPS has been formulated in latent space by redefining the measurement likelihood as

$$p(y \mid z_t) \approx p\big(y \,\big|\, \hat{x}_0 = \mathcal{D}\big(\mathbb{E}[z_0 \mid z_t]\big)\big)\,.$$

This straightforward formulation, commonly referred to as Latent DPS, has been observed to introduce artifacts, largely due to the nonlinearity of the decoder. To mitigate this effect, [28] proposed a regularization term encouraging the latent variables to remain close to a fixed point of the encoder–decoder mapping, while [32] enforced data consistency during optimization followed by a projection of the latent variables back onto the noisy manifold.

3 Proposed Approach

Given a noisy observation $y \in \mathbb{R}^m$ of an unknown signal $x \in \mathbb{R}^k$, our goal is to sample from $p_\theta(x_0 \mid y)$ using a pretrained diffusion or flow-based models. We aim to apply the REPA framework to inverse problems. However, a key challenge is that representation alignment requires access to the ground-truth signal, which is not available in this setting. To overcome this, we must choose an alternative input to the DINOv2 encoder that can stand in for the missing ground truth. In particular, we need an approximation $\bar{x}_0$ of the unknown x_0 that produces a *proxy representation* $c_{\text{proxy}} \in \mathbb{R}^{N \times D_1}$, where N denotes the number of patch tokens and D_1 is their feature dimension. This representation should satisfy

$$c_{\text{proxy}} \equiv f_{\text{DINOv2}}(\bar{x}_0) \approx f_{\text{DINOv2}}(x_0). \tag{6}$$

We then introduce a *tilted distribution*, [23], that incorporates representation alignment as reward:

$$\widetilde{p}(x_t \mid y) \propto p(y \mid x_t)\, p_t(x_t) \exp\big(\lambda\, \text{REPA}(\bar{x}_0, h_t)\big), \tag{7}$$

where $h_t = \text{DIFFENC}(x_t, t)$ denotes the intermediate diffusion representation and $\lambda > 0$ controls the strength of the alignment term. The likelihood $p(y \mid x_t)$ enforces measurement consistency, while $p_t(x_t)$ corresponds to the unconditional prior induced by the generative model. The REPA term defined in Eq. (5) encourages alignment between the diffusion representation of x_t and the proxy DINOv2 features, thereby biasing the sampling process toward semantically consistent reconstructions.

On the selection of c_{proxy}. To address the fact that representation alignment [42] is not directly applicable to inverse problems where the ground-truth image is unavailable at inference time, we construct c_{proxy} from an approximate reconstruction. We initialize the proxy using the DINOv2 features of the available observation and, as the reverse diffusion process progresses and the reconstruction becomes more informative, we gradually replace this proxy with the features of the model's current denoised estimate, namely $f_{\text{DINOv2}}(\mathbb{E}[x_0 \mid x_t])$. In both cases, we rely on the robustness of pretrained DINOv2 features, which, as shown in our experiments, remain stable under the degradations present in super-resolution and deblurring tasks. An ablation in Appendix A.4 quantifies the reliability of this proxy across tasks. We further compare against alternative encoders, such as CLIP [25], in Appendix A.6, where DINOv2 consistently yields improved performance. We also examine the behavior of the method across a broader range of degradation levels in Appendix A.7, where the proxy-based alignment remains effective even in more challenging settings.

On the availability of the alignment mapping. The regularizer in (7) relies on a projection head g_ϕ mapping diffusion representations into the DINOv2 feature space. For models trained with representation alignment, this mapping is available from pretraining. More generally, our framework can also be applied to arbitrary pretrained diffusion models by learning a post-hoc mapping between diffusion representations and DINOv2 features while keeping the diffusion model itself frozen. Since only the projection head g_ϕ is optimized, this additional training is lightweight and inexpensive, compared to diffusion-model pretraining. We refer the reader to Appendix A.14 for further details. As we show in Appendix A.15, this post-hoc adaptation preserves the benefits of representation alignment for inverse problems and enables REPA regularization to be used with existing generative models not previously pretrained with REPA.

Extension to latent diffusion models. The proposed representation-alignment strategy applies naturally to latent diffusion models. Let z_t denote the latent state at timestep t. In this setting, the tilted distribution becomes

$$\widetilde{p}(z_t \mid y) \propto p(y \mid z_t) p_t(z_t) \exp\left(\lambda \textsc{Repa}(\bar{x}_0, h_t)\right),$$

With a slight abuse of notation, we use DIFFENC to denote the diffusion encoder in both pixel-space and latent-space models, and write $h_t = \textsc{DiffEnc}(z_t, t)$ for latent diffusion.

Our general algorithm for a latent-space velocity-based sampler is summarized in Algorithm 1. Step 6 is intentionally kept abstract; as discussed in Section 2.3, different inverse-problem solvers approximate this term in different ways. The proposed regularizer is compatible with standard diffusion-based reconstruction pipelines. In our experiments, we instantiate the framework using two state-of-the-art latent diffusion methods, with further implementation details provided in Appendix A.2 and Appendix A.3. We further provide an ablation study in Appendix A.10 analyzing the effect of all hyperparameters of our framework, including the cutoff timestep.

Algorithm 1 REPA-regularized Inverse Algorithm

Require: Flow or diffusion model u_θ, measurement y, learning rate η, regularizer strength λ, proxy representation c_{proxy}, timestep t_{cutoff}, Decoder $\mathcal{D}$, Initialize $z_T \sim \mathcal{N}(0, I)$,

1: **for** $t = T, \dots, 1$ **do**
2: $\quad z_{t-1} \leftarrow z_t - \frac{1}{T} \cdot u_\theta(z_t, t) + \eta \nabla_{z_t} \log p(y \mid z_t)$
3: $\quad z_{t-1} \leftarrow z_{t-1} + \lambda \nabla_{z_t} \sum_{n=1}^{N} \cos\big(c_{\text{proxy}}^{[n]}, g_\phi(\text{DiffEnc}^{[n]}(z_t, t))\big)$
4: $\quad$ **if** $t < t_{\text{cutoff}}$ **then**
5: $\quad\quad c_{\text{proxy}} \leftarrow f_{\text{DINOv2}}\big(\mathcal{D}(\mathbb{E}[z_0 \mid z_t])\big)$
6: $\quad$ **end if**
7: **end for**
8: **return** z_0

4 Theoretical Results

Recent advances in generative modeling have demonstrated that objectives defined in deep feature spaces, rather than purely pixel-based discrepancies, produce reconstructions that better capture perceptual similarity [9, 44, 10]. Motivated by this observation, our goal in this section is to clarify how the REPA regularizer fits within this broader class of feature-based objectives. In

particular, we present two theoretical results that characterize how REPA acts on (i) the DINOv2-space representations of reconstructed images and (ii) the latent diffusion state itself.

First, we show that maximizing the REPA objective encourages alignment between the DINOv2 feature distributions of reconstructed and ground-truth images, yielding an interpretation in terms of maximum mean discrepancy (MMD). Second, we study how REPA affects the latent states of the diffusion model during the reverse process. Under suitable assumptions, we show that a REPA update moves the current diffusion state toward the latent representation of the clean image. This provides a complementary view: REPA influences not only the DINOv2 representation of the reconstruction but also the latent state that guides the sampling trajectory.

Before presenting the main results, we introduce two quantities that capture, respectively, the alignment between feature spaces and the accuracy of the proxy representations used in our analysis.

Definition 4.1 (Misalignment between DINOv2 and diffusion representations)**.** For an image x and diffusion timestep t, we define the representation misalignment as

$$\mathrm{MisREPA}(x,t) := \mathbb{E}_n \, \| f^{[n]}_{\mathrm{DINOv2}}(x) - g_\phi(\mathrm{DiffEnc}^{[n]}(x,t)) \|_2^2,$$

where the expectation is taken uniformly over patch indices $n \in \{1,\dots,N\}$. Here $f^{[n]}_{\mathrm{DINOv2}}(x)$ and $\mathrm{DiffEnc}^{[n]}(x,t)$ denote the n-th patch features from the DINOv2 encoder and the diffusion model encoder, respectively. The mapping g_ϕ is the projection head introduced in Section 2.2[1].

Definition 4.2 (Proxy approximation error)**.** For a ground-truth image x and its proxy approximation $\bar{x}$ (defined in Section 3), we define the proxy approximation error as

$$\mathrm{ApproxErr}(x,\bar{x}) := \mathbb{E}_n \left\| f^{[n]}_{\mathrm{DINOv2}}(x) - f^{[n]}_{\mathrm{DINOv2}}(\bar{x}) \right\|_2^2,$$

where the expectation is taken uniformly over patch indices $n \in \{1,\dots,N\}$.

In practice, both quantities defined above are typically small. The feature misalignment $\mathrm{MisREPA}(x,t)$ is mitigated through the explicit alignment of DINOv2 and diffusion encoder representations during training [42], while the approximation error $\mathrm{ApproxErr}(x,\bar{x})$ is reduced by constructing proxy features $\bar{x}$ that serves as reliable substitutes for the unavailable ground-truth features (see Section 3). Robustness of DINOv2 features to common image degradations [22], ensures that the resulting approximation gap remains small across the inverse problems we study.

Feature-Space Alignment: REPA as an MMD Surrogate. Building on the definitions introduced above, we now establish a connection between the REPA regularizer and the statistical discrepancy between DINOv2 features of clean and reconstructed images.

Proposition 4.3. *Assume $x \sim p_X$ is a ground-truth image and $\hat{x} \sim p_{\hat{X}|Y}$ is its corresponding reconstruction, where $p_{\hat{X}|Y}$ is the distribution induced by any reconstruction method. Assume further that all DINOv2 feature embeddings are ℓ_2–normalized. Let $\bar{x}$ be a proxy approximation of x. Define the empirical mean DINOv2 feature embedding as $\mu_f(x) := \mathbb{E}_n\left[f^{[n]}_{\mathrm{DINOv2}}(x)\right]$. Then the expected REPA alignment satisfies*

$$\mathbb{E}_{\hat{x},\bar{x}}[\textit{REPA}(\bar{x},\hat{x})] \le 1 - \tfrac{1}{8}\,\mathrm{MMD}_{\mathrm{DINOv2}}\big(p_X, p_{\hat{X}}\big) + \tfrac{1}{2}\,\mathbb{E}_{x,\bar{x}}[\mathrm{ApproxErr}(x,\bar{x})] + \tfrac{1}{4}\,\mathbb{E}_{\hat{x}}[\mathrm{MisREPA}(\hat{x})]\,.$$

where $\mathrm{MMD}_{\mathrm{DINOv2}}\big(p_X,\, p_{\hat{X}}\big) = \left\|\mathbb{E}_x[\mu_f(x)] - \mathbb{E}_{\hat{x}}[\mu_f(\hat{x})]\right\|_2^2$ is the maximum mean discrepancy between p_X and $p_{\hat{X}}$ in the DINOv2 feature space.

The proof is provided in the Appendix A.1. Proposition 4.3 establishes a connection between the representation alignment term and the maximum mean discrepancy (MMD) [2], which quantifies perceptual divergence between feature distributions. This relationship indicates that *maximizing* the REPA term encourages the *minimization* of a divergence measure captured by the MMD together with additional penalties accounting for feature misalignment between diffusion and DINOv2 representations, as well as an approximation error arising from the use of proxy rather than ground-truth features for alignment.

When these terms are sufficiently small, Proposition 4.3 implies that maximizing the REPA term effectively corresponds to minimizing the maximum mean discrepancy (MMD) between the DINOv2

[1]When the timestep argument is omitted, all t-dependent quantities are evaluated at $t = 0$. In particular, $\mathrm{MisREPA}(x) \equiv \mathrm{MisREPA}(x,0)$ and $\mathrm{DiffEnc}^{[n]}(x) \equiv \mathrm{DiffEnc}^{[n]}(x,0)$.



Figure 2: Qualitative comparison of inverse problem reconstruction with and without REPA. The top block corresponds to box inpainting and the bottom block to Gaussian deblurring; Within each panel, the first row corresponds to Latent DPS and the second row to ReSample.

feature distributions of reconstructed and ground-truth images. This interpretation reveals that REPA regularization offers a principled, representation-based mechanism for enforcing perceptual consistency.

Effect of REPA on Diffusion Representations. We now study how a single REPA update influences the latent diffusion state relative to that of the clean image.

Proposition 4.4 (informal)**.** *Consider an inverse problem with observation $y \in \mathbb{R}^m$ generated from a clean image $x \sim p_X$, and let $\bar{x}$ denote the proxy used by REPA. Let $z_t \in \mathbb{R}^d$ be the diffusion state at time t, $z_t^{(\mathrm{REPA})}$ its REPA-regularized update. Let $z^* \in \mathbb{R}^d$ denote the latent variable associated with the clean image x. Under regularity assumptions on the Jacobian of the diffusion encoder J_{DiffEnc} and the mapping g_ϕ (see Appendix A.2), there exists a radius $r > 0$ such that, whenever $\|z_t - z^*\|_2 < r$, the REPA update induces a contraction in the diffusion state space. In particular,*

$$\|z_t^{(\mathrm{REPA})} - z^*\|_2 \le C_1 \|z_t - z^*\|_2 + e(x), \quad e(x) := C_2 \left(\sqrt{\mathrm{ApproxErr}(x, \bar{x})} + \sqrt{\mathrm{MisREPA}(x)} \right),$$

where $C_1 \in (0, 1)$ and $C_2 > 0$ are constants that depend on the conditioning of J_{DiffEnc} and g_ϕ.

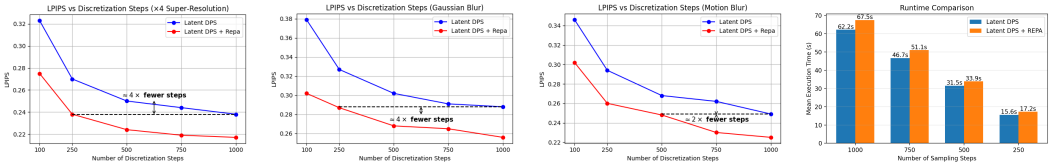
The proof is provided in Appendix A.1. Proposition 4.4 characterizes how the REPA update modifies the latent diffusion state. The inequality shows that, when the current state z_t is reasonably close to the clean latent code z^*, a single REPA step contracts their distance up to two additive terms: the proxy approximation error and the representation misalignment, both of which are expected to be small in practice. This contraction therefore holds in a local regime around z^*, which corresponds in practice to stages of the diffusion process where the global structure of the reconstruction is already correct and the remaining errors are primarily fine-scale details and artifacts. In this regime, REPA acts as a perceptual regularizer, refining local image details and correcting artifacts that are not effectively addressed by the baseline update alone. Qualitative examples illustrating this behavior are provided in Figure 2 and the Appendix A.16.

5 Experimental Results

In this section, we present experimental results demonstrating the effectiveness of our alignment regularizer. We evaluate reconstruction quality using four widely adopted metrics: PSNR (peak

Table 1: Performance comparison on ImageNet and FFHQ across inverse tasks.

Task	Method	ImageNet				FFHQ			
		LPIPS↓	FID↓	PSNR↑	SSIM↑	LPIPS↓	FID↓	PSNR↑	SSIM↑
4× SR	Latent DPS	0.238	123.82	26.88	0.732	0.188	56.69	28.99	0.814
	Latent DPS + REPA	0.217	86.88	26.82	0.731	0.176	51.27	29.12	0.819
	Resample	0.208	97.02	26.70	0.736	0.178	52.82	29.06	0.814
	Resample + REPA	**0.197**	**74.70**	26.99	0.740	**0.167**	**46.36**	**29.17**	0.818
	DPS	0.244	92.13	24.42	0.681	0.182	54.19	27.67	0.804
	Latent DAPS	0.252	120.57	**27.13**	**0.744**	0.206	74.82	28.95	**0.820**
Inpainting	Latent DPS	0.151	116.53	20.53	0.822	0.192	65.89	23.55	0.785
	Latent DPS + REPA	**0.139**	88.69	20.45	0.824	**0.178**	**57.04**	23.83	0.784
	Resample	0.153	121.98	20.53	0.812	0.192	67.99	23.86	0.792
	Resample + REPA	0.143	**87.15**	20.79	**0.827**	**0.178**	61.97	24.01	0.793
	DPS	0.191	97.95	19.11	0.769	0.190	104.53	20.02	0.786
	Latent DAPS	0.318	188.44	**21.21**	0.718	0.210	89.21	**24.39**	**0.817**
Gaussian Deblur	Latent DPS	0.288	152.96	25.76	0.648	0.192	60.65	28.15	0.783
	Latent DPS + REPA	0.256	102.99	25.66	0.669	0.186	55.53	28.21	0.787
	Resample	0.259	115.47	26.19	0.699	0.172	56.41	27.01	0.753
	Resample + REPA	**0.223**	**89.67**	**26.49**	**0.707**	**0.168**	**52.73**	27.17	0.756
	DPS	0.366	157.73	19.55	0.461	0.177	53.18	27.19	0.789
	Latent DAPS	0.291	159.67	26.02	0.692	0.229	104.43	**28.73**	**0.809**
Motion Deblur	Latent DPS	0.249	129.08	27.19	0.738	0.170	52.14	27.20	0.773
	Latent DPS + REPA	0.225	90.23	27.01	0.735	0.165	47.18	27.16	0.772
	Resample	0.210	89.95	27.57	0.739	0.157	52.19	28.36	0.791
	Resample + REPA	**0.192**	**75.11**	**27.80**	**0.766**	0.151	50.02	28.41	0.794
	DPS	0.242	89.06	24.17	0.678	**0.146**	**43.32**	27.28	0.793
	Latent DAPS	0.264	125.18	27.25	0.744	0.191	76.21	**29.77**	**0.836**



(a) Super Resolution (b) Gaussian Deblurring (c) Motion Deblurring (d) Runtime Comparison

Figure 3: Comparison of LPIPS as a function of sampling steps, together with runtime comparison.

signal-to-noise ratio), SSIM (structural similarity index) [37], LPIPS (learned perceptual image patch similarity) [44], and FID (Fréchet Inception Distance) [11]. Experiments are conducted on both the ImageNet and FFHQ datasets [7, 15], with FFHQ images resized to 256×256. All metrics for both datasets are averaged over 100 images from their corresponding validation splits.

We consider four inverse problems: super-resolution, box inpainting, Gaussian deblurring, and motion deblurring. Following the standard corruption operators used in state-of-the-art diffusion-based inverse problem methods [5, 43] we adopt the same degradation models in our experiments. For super-resolution, images are downsampled by a factor of 4. For box inpainting, we mask out a 128×128 square region. Gaussian deblurring is performed using a 61×61 kernel with standard deviation 3.0. Motion blur is simulated using a kernel with size 61×61 and intensity 0.5. For ImageNet we use additive Gaussian noise with standard deviation 0.01. For FFHQ we increase the noise level to 0.05 in order to obtain a more challenging reconstruction setting. We also include results about two non-linear inverse problems for the ImageNet dataset in Appendix A.8.

5.1 Effectiveness of the REPA Regularizer

This subsection evaluates how the REPA regularizer influences reconstruction quality by applying it to two representative latent-space solvers. To this end, we instantiate Algorithm 1 with Latent

DPS and ReSample [32]. A detailed description of these methods and their integration with REPA is provided in Appendix A.2. For ImageNet experiments, we use the latent diffusion model trained with representation alignment from [42], together with its pretrained MLP that projects diffusion representations into the DINOv2 space. For FFHQ, we train a representation-aligned SIT-BASE model from scratch following the same setup as [42]. In ImageNet experiments, the regularizer is applied to representations extracted after the eighth transformer block, while for FFHQ it is applied after the fourth block, we include an ablation study about this choice in Appendix A.9. Our approach can be extended to independently pretrained diffusion models by learning a mapping between the diffusion representations and the DINOv2 feature space. We study this setting in Appendix A.15. In this case, incorporating the REPA regularizer continues to provide perceptual improvements for inverse problems. In line with our theory, the method remains effective as long as the learned mapping is sufficiently accurate, corresponding to a low $\mathrm{MisREPA}$ error.

Table 1 reports quantitative results across all four inverse problems. Incorporating REPA yields consistent improvements in perceptual metrics, notably reducing LPIPS and FID for both Latent DPS and ReSample while maintaining comparable PSNR and SSIM values. PSNR and SSIM remain comparable to the baseline, while perceptual metrics consistently improve. This behaviour is in line with the perception–distortion trade-off, whereby improvements in perceptual realism do not necessarily translate to gains in pixel-wise metrics. We include qualitative results in Appendix A.12 illustrating this phenomenon. These results suggest that representation alignment guides the diffusion trajectory toward semantically consistent and perceptually realistic reconstructions that better match the target image. Figure 2 presents qualitative comparisons for box inpainting and Gaussian deblurring, where reconstructions obtained with REPA are visually sharper and more faithful to the ground truth. In addition to improving these latent solvers, we also compare our approach with other state-of-the-art reconstruction algorithms. For pixel-space methods, we consider DPS [5], evaluated using the pretrained diffusion model from [8]. For latent diffusion baselines, we include Latent DAPS, implemented with the conditional ImageNet latent diffusion model from [27]. As shown in Table 1, the proposed alignment regularizer consistently achieves state-of-the-art performance in perception-based metrics across the considered inverse problems.

Effect of REPA with Varying Discretization Steps. Figure 3 illustrates how LPIPS varies with the number of discretization steps across three inverse problems, together with the corresponding runtime comparison. Incorporating the REPA regularizer consistently reduces perceptual error compared to Latent DPS alone. More importantly, REPA enables comparable or better perceptual quality with substantially fewer sampling steps: for example, in super-resolution and Gaussian deblurring, REPA achieves the same LPIPS with roughly $4\times$ fewer steps, while in motion deblurring it achieves the same level with about $2\times$ fewer steps. The fourth plot in Figure 3 shows the runtime comparison for different numbers of discretization steps. The reported runtime is averaged over 100 images for the super resolution problem. While REPA introduces additional computation per step, the reduced number of required sampling steps allows the method to reach the same perceptual quality in less overall runtime. All runtime experiments were run on a single NVIDIA L40 GPU (48GB).

REPA vs Guidance in the DINO feature space. To further showcase the benefits of representation alignment, Appendix A.13 compares REPA to a variant that enforces consistency directly in the DINOv2 feature space of the reconstructed image. Concretely, the feature-only variant applies the following guidance at each timestep:

$$z_{t-1} \leftarrow z_{t-1} + \lambda \nabla_{z_t} \sum_{n=1}^{N} \cos\Big(c_{\text{proxy}}^{[n]}, f_{\text{DINOv2}}^{[n]}\big(\mathcal{D}(\mathbb{E}[z_0 \mid z_t])\big)\Big),$$

This approach relies solely on the DINOv2 features of the decoded image. In contrast, REPA aligns the model's internal representations with DINOv2 features. As observed in Appendix A.13, this feature-only guidance performs worse in practice. A natural explanation through the lens of Proposition 4.4 is that the composite mapping $z_t \mapsto \mathcal{D}(\mathbb{E}[z_0 \mid z_t]) \mapsto f_{\text{DINOv2}}(\cdot)$ is significantly more ill-conditioned than the lightweight projection used in REPA, resulting in weaker and less stable gradients with respect to the diffusion state.

6 Conclusions

In this work, we introduced *representation alignment* for solving inverse problems with diffusion- and flow-based generative models. By aligning internal model representations with features from

a pretrained DINOv2 encoder, our method provides a strong semantic prior that guides the reconstruction process toward perceptually meaningful solutions. We further offered theoretical insights into this mechanism, showing that REPA regularization corresponds to minimizing a divergence in the DINOv2 feature space and reduces the discrepancy between the current and the clean latent state. These results elucidate why alignment can enhance perceptual fidelity in inverse problem settings. Overall, our study demonstrates that representation alignment constitutes an effective tool for improving generative inverse problem solvers, yielding benefits at inference time.

References

[1] Michael S Albergo, Nicholas M Boffi, and Eric Vanden-Eijnden. Stochastic interpolants: A unifying framework for flows and diffusions. *arXiv preprint arXiv:2303.08797*, 2023.

[2] Michael Arbel, Anna Korba, Adil Salim, and Arthur Gretton. Maximum mean discrepancy gradient flow. *Advances in Neural Information Processing Systems*, 32, 2019.

[3] Mahmoud Assran, Quentin Duval, Ishan Misra, Piotr Bojanowski, Pascal Vincent, Michael Rabbat, Yann LeCun, and Nicolas Ballas. Self-supervised learning from images with a joint-embedding predictive architecture. In *Proceedings of the IEEE/CVF Conference on Computer Vision and Pattern Recognition*, pages 15619–15629, 2023.

[4] Andreas Blattmann, Robin Rombach, Kaan Oktay, Jonas Müller, and Björn Ommer. Retrieval-augmented diffusion models. *Advances in Neural Information Processing Systems*, 35:15309–15324, 2022.

[5] Hyungjin Chung, Jeongsol Kim, Michael Thompson Mccann, Marc Louis Klasky, and Jong Chul Ye. Diffusion posterior sampling for general noisy inverse problems. In *The Eleventh International Conference on Learning Representations*, 2023.

[6] Giannis Daras, Hyungjin Chung, Chieh-Hsin Lai, Yuki Mitsufuji, Jong Chul Ye, Peyman Milanfar, Alexandros G Dimakis, and Mauricio Delbracio. A survey on diffusion models for inverse problems. *arXiv preprint arXiv:2410.00083*, 2024.

[7] Jia Deng, Wei Dong, Richard Socher, Li-Jia Li, Kai Li, and Li Fei-Fei. Imagenet: A large-scale hierarchical image database. In *2009 IEEE conference on computer vision and pattern recognition*, pages 248–255. Ieee, 2009.

[8] Prafulla Dhariwal and Alexander Nichol. Diffusion models beat gans on image synthesis. *Advances in neural information processing systems*, 34:8780–8794, 2021.

[9] Alexey Dosovitskiy and Thomas Brox. Generating images with perceptual similarity metrics based on deep networks. *Advances in Neural Information Processing Systems*, 29, 2016.

[10] Stephanie Fu, Netanel Tamir, Shobhita Sundaram, Lucy Chai, Richard Zhang, Tali Dekel, and Phillip Isola. Dreamsim: Learning new dimensions of human visual similarity using synthetic data. *arXiv preprint arXiv:2306.09344*, 2023.

[11] Martin Heusel, Hubert Ramsauer, Thomas Unterthiner, Bernhard Nessler, and Sepp Hochreiter. Gans trained by a two time-scale update rule converge to a local nash equilibrium. *Advances in neural information processing systems*, 30, 2017.

[12] Jonathan Ho, Ajay Jain, and Pieter Abbeel. Denoising diffusion probabilistic models. *Advances in neural information processing systems*, 33:6840–6851, 2020.

[13] Vincent Tao Hu, David W Zhang, Yuki M Asano, Gertjan J Burghouts, and Cees GM Snoek. Self-guided diffusion models. In *Proceedings of the IEEE/CVF Conference on Computer Vision and Pattern Recognition*, pages 18413–18422, 2023.

[14] Aapo Hyvärinen and Peter Dayan. Estimation of non-normalized statistical models by score matching. *Journal of Machine Learning Research*, 6(4), 2005.

[15] Tero Karras, Samuli Laine, and Timo Aila. A style-based generator architecture for generative adversarial networks. In *Proceedings of the IEEE/CVF conference on computer vision and pattern recognition*, pages 4401–4410, 2019.

[16] Chieh-Hsin Lai, Yang Song, Dongjun Kim, Yuki Mitsufuji, and Stefano Ermon. The principles of diffusion models. *arXiv preprint arXiv:2510.21890*, 2025.

[17] Xingjian Leng, Jaskirat Singh, Yunzhong Hou, Zhenchang Xing, Saining Xie, and Liang Zheng. Repa-e: Unlocking vae for end-to-end tuning with latent diffusion transformers. *arXiv preprint arXiv:2504.10483*, 2025.

[18] Alexander C Li, Mihir Prabhudesai, Shivam Duggal, Ellis Brown, and Deepak Pathak. Your diffusion model is secretly a zero-shot classifier. In *Proceedings of the IEEE/CVF International Conference on Computer Vision*, pages 2206–2217, 2023.

[19] Tianhong Li, Dina Katabi, and Kaiming He. Return of unconditional generation: A self-supervised representation generation method. *Advances in Neural Information Processing Systems*, 37:125441–125468, 2024.

[20] Yaron Lipman, Ricky TQ Chen, Heli Ben-Hamu, Maximilian Nickel, and Matt Le. Flow matching for generative modeling. In *11th International Conference on Learning Representations, ICLR 2023*, 2023.

[21] Xingchao Liu, Chengyue Gong, and Qiang Liu. Flow straight and fast: Learning to generate and transfer data with rectified flow. In *The Eleventh International Conference on Learning Representations (ICLR)*, 2023.

[22] Maxime Oquab, Timothée Darcet, Théo Moutakanni, Huy Vo, Marc Szafraniec, Vasil Khalidov, Pierre Fernandez, Daniel Haziza, Francisco Massa, Alaaeldin El-Nouby, et al. Dinov2: Learning robust visual features without supervision. *arXiv preprint arXiv:2304.07193*, 2023.

[23] Jean Pachebat, Giovanni Conforti, Alain Durmus, and Yazid Janati. Iterative tilting for diffusion fine-tuning. *arXiv preprint arXiv:2512.03234*, 2025.

[24] Maitreya Patel, Song Wen, Dimitris N Metaxas, and Yezhou Yang. Steering rectified flow models in the vector field for controlled image generation. *arXiv preprint arXiv:2412.00100*, 2024.

[25] Alec Radford, Jong Wook Kim, Chris Hallacy, Aditya Ramesh, Gabriel Goh, Sandhini Agarwal, Girish Sastry, Amanda Askell, Pamela Mishkin, Jack Clark, et al. Learning transferable visual models from natural language supervision. In *International conference on machine learning*, pages 8748–8763. PMLR, 2021.

[26] Ron Raphaeli, Sean Man, and Michael Elad. Silo: Solving inverse problems with latent operators. In *Proceedings of the IEEE/CVF International Conference on Computer Vision*, pages 10570–10580, 2025.

[27] Robin Rombach, Andreas Blattmann, Dominik Lorenz, Patrick Esser, and Björn Ommer. High-resolution image synthesis with latent diffusion models. In *Proceedings of the IEEE/CVF conference on computer vision and pattern recognition*, pages 10684–10695, 2022.

[28] Litu Rout, Negin Raoof, Giannis Daras, Constantine Caramanis, Alex Dimakis, and Sanjay Shakkottai. Solving linear inverse problems provably via posterior sampling with latent diffusion models. In *Thirty-seventh Conference on Neural Information Processing Systems*, 2023.

[29] Shelly Sheynin, Oron Ashual, Adam Polyak, Uriel Singer, Oran Gafni, Eliya Nachmani, and Yaniv Taigman. Knn-diffusion: Image generation via large-scale retrieval. *arXiv preprint arXiv:2204.02849*, 2022.

[30] Oriane Siméoni, Huy V Vo, Maximilian Seitzer, Federico Baldassarre, Maxime Oquab, Cijo Jose, Vasil Khalidov, Marc Szafraniec, Seungeun Yi, Michaël Ramamonjisoa, et al. Dinov3. *arXiv preprint arXiv:2508.10104*, 2025.

[31] Jascha Sohl-Dickstein, Eric Weiss, Niru Maheswaranathan, and Surya Ganguli. Deep unsupervised learning using nonequilibrium thermodynamics. In *International conference on machine learning*, pages 2256–2265. PMLR, 2015.

[32] Bowen Song, Soo Min Kwon, Zecheng Zhang, Xinyu Hu, Qing Qu, and Liyue Shen. Solving inverse problems with latent diffusion models via hard data consistency. In *The Twelfth International Conference on Learning Representations*, 2024.

[33] Jiaming Song, Chenlin Meng, and Stefano Ermon. Denoising diffusion implicit models. In *International Conference on Learning Representations*, 2021.

[34] Darshan Thaker, Abhishek Goyal, and René Vidal. Frequency-guided posterior sampling for diffusion-based image restoration. In *Proceedings of the IEEE/CVF International Conference on Computer Vision*, pages 12873–12882, 2025.

[35] Yuchuan Tian, Hanting Chen, Mengyu Zheng, Yuchen Liang, Chao Xu, and Yunhe Wang. U-repa: Aligning diffusion u-nets to vits. *arXiv preprint arXiv:2503.18414*, 2025.

[36] Chenyu Wang, Cai Zhou, Sharut Gupta, Zongyu Lin, Stefanie Jegelka, Stephen Bates, and Tommi Jaakkola. Learning diffusion models with flexible representation guidance. *arXiv preprint arXiv:2507.08980*, 2025.

[37] Zhou Wang, Alan C Bovik, Hamid R Sheikh, and Eero P Simoncelli. Image quality assessment: from error visibility to structural similarity. *IEEE transactions on image processing*, 13(4):600–612, 2004.

[38] Ziqiao Wang, Wangbo Zhao, Yuhao Zhou, Zekai Li, Zhiyuan Liang, Mingjia Shi, Xuanlei Zhao, Pengfei Zhou, Kaipeng Zhang, Zhangyang Wang, et al. Repa works until it doesn't: Early-stopped, holistic alignment supercharges diffusion training. *arXiv preprint arXiv:2505.16792*, 2025.

[39] Weilai Xiang, Hongyu Yang, Di Huang, and Yunhong Wang. Denoising diffusion autoencoders are unified self-supervised learners. In *Proceedings of the IEEE/CVF International Conference on Computer Vision*, 2023.

[40] Wanghan Xu, Xiaoyu Yue, Zidong Wang, Yao Teng, Wenlong Zhang, Xihui Liu, Luping Zhou, Wanli Ouyang, and Lei Bai. Exploring representation-aligned latent space for better generation. *arXiv preprint arXiv:2502.00359*, 2025.

[41] Jingfeng Yao, Bin Yang, and Xinggang Wang. Reconstruction vs. generation: Taming optimization dilemma in latent diffusion models. In *Proceedings of the Computer Vision and Pattern Recognition Conference*, pages 15703–15712, 2025.

[42] Sihyun Yu, Sangkyung Kwak, Huiwon Jang, Jongheon Jeong, Jonathan Huang, Jinwoo Shin, and Saining Xie. Representation alignment for generation: Training diffusion transformers is easier than you think. *arXiv preprint arXiv:2410.06940*, 2024.

[43] Bingliang Zhang, Wenda Chu, Julius Berner, Chenlin Meng, Anima Anandkumar, and Yang Song. Improving diffusion inverse problem solving with decoupled noise annealing. In *Proceedings of the Computer Vision and Pattern Recognition Conference*, pages 20895–20905, 2025.

[44] Richard Zhang, Phillip Isola, Alexei A Efros, Eli Shechtman, and Oliver Wang. The unreasonable effectiveness of deep features as a perceptual metric. In *Proceedings of the IEEE conference on computer vision and pattern recognition*, pages 586–595, 2018.

A Appendix

A.1 Proofs

Proposition A.1. *Assume $x \sim p_X$ is a ground-truth image and $\hat{x} \sim p_{\hat{X}|Y}$ is its corresponding reconstruction, where $p_{\hat{X}|Y}$ is the distribution induced by any reconstruction method. Assume further that all DINOv2 feature embeddings are ℓ_2–normalized. Let $\bar{x}$ be a proxy approximation of x Define the empirical mean DINOv2 feature embedding as*

$$\mu_f(x) := \mathbb{E}_n \left[f^{[n]}_{\mathrm{DINOv2}}(x) \right].$$

Then the expected REPA alignment satisfies

$$\mathbb{E}_{\hat{x},\bar{x}}[\textit{REPA}(\bar{x},\hat{x})] \;\le\; 1 - \frac{1}{8}\,\mathrm{MMD}_{\mathrm{DINOv2}}\big(p_X,\, p_{\hat{X}}\big) + \frac{1}{2}\,\mathbb{E}_{x,\bar{x}}\big[\mathrm{ApproxErr}(x,\bar{x})\big] + \frac{1}{4}\,\mathbb{E}_{\hat{x}}\big[\mathrm{MisREPA}(\hat{x})\big].$$

where

$$\mathrm{MMD}_{\mathrm{DINOv2}}\big(p_X,\, p_{\hat{X}}\big) = \big\|\mathbb{E}_x[\mu_f(x)] - \mathbb{E}_{\hat{x}}[\mu_f(\hat{x})]\big\|_2^2$$

is the maximum mean discrepancy between p_X and $p_{\hat{X}}$ in the DINOv2 feature space.

Proof.

$$\mathrm{REPA}(\bar{x},\hat{x}) = \frac{1}{N}\sum_{n=1}^{N}\cos\Big(f^{[n]}_{\mathrm{DINOv2}}(\bar{x}),\, g_\phi\big(\textsc{DiffEnc}^{[n]}(\hat{x})\big)\Big),$$

Assume the features are ℓ_2–normalized. Then for each n,

$$\cos\Big(f^{[n]}_{\mathrm{DINOv2}}(\bar{x}),\, g_\phi\big(\textsc{DiffEnc}^{[n]}(\hat{x})\big)\Big) = 1 - \tfrac{1}{2}\,\big\|f^{[n]}_{\mathrm{DINOv2}}(\bar{x}) - g_\phi(\textsc{DiffEnc}^{[n]}(\hat{x}))\big\|_2^2,$$

and hence

$$\mathrm{REPA}(\bar{x},\hat{x}) = 1 \;-\; \frac{1}{2N}\sum_{n=1}^{N}\big\|f^{[n]}_{\mathrm{DINOv2}}(\bar{x}) - g_\phi(\textsc{DiffEnc}^{[n]}(\hat{x}))\big\|_2^2.$$

Let the empirical (mean) feature embeddings be

$$\mu_f(x) := \frac{1}{N}\sum_{n=1}^{N} f^{[n]}_{\mathrm{DINOv2}}(x), \qquad \mu_f(\bar{x}) := \frac{1}{N}\sum_{n=1}^{N} f^{[n]}_{\mathrm{DINOv2}}(\bar{x}),$$

$$\mu_f(\hat{x}) := \frac{1}{N}\sum_{n=1}^{N} f^{[n]}_{\mathrm{DINOv2}}(\hat{x}), \qquad \mu_g(\hat{x}) := \frac{1}{N}\sum_{n=1}^{N} g_\phi(\textsc{DiffEnc}^{[n]}(\hat{x})).$$

From Jensen's inequality for the squared norm :

$$\big\|\mu_f(x) - \mu_f(\hat{x})\big\|_2^2 \le 2\,\big\|\mu_f(x) - \mu_g(\hat{x})\big\|_2^2 + 2\,\big\|\mu_f(\hat{x}) - \mu_g(\hat{x})\big\|_2^2.$$

Moreover,

$$\big\|\mu_f(x) - \mu_g(\hat{x})\big\|_2^2 = \Big\|\frac{1}{N}\sum_{n=1}^{N}\big(f^{[n]}_{\mathrm{DINOv2}}(x) - g_\phi(\textsc{DiffEnc}^{[n]}(\hat{x}))\big)\Big\|_2^2 \;\le\; \frac{1}{N}\sum_{n=1}^{N}\big\|f^{[n]}_{\mathrm{DINOv2}}(x) - g_\phi(\textsc{DiffEnc}^{[n]}(\hat{x}))\big\|_2^2,$$

and similarly

$$\big\|\mu_f(\hat{x}) - \mu_g(\hat{x})\big\|_2^2 \;\le\; \frac{1}{N}\sum_{n=1}^{N}\big\|f^{[n]}_{\mathrm{DINOv2}}(\hat{x}) - g_\phi(\textsc{DiffEnc}^{[n]}(\hat{x}))\big\|_2^2 \;= \mathrm{MisREPA}(\hat{x}).$$

Combining the two yields

$$\big\|\mu_f(x) - \mu_f(\hat{x})\big\|_2^2 \le \frac{2}{N}\sum_{n=1}^{N}\big\|f^{[n]}_{\mathrm{DINOv2}}(x) - g_\phi(\textsc{DiffEnc}^{[n]}(\hat{x}))\big\|_2^2 + 2\,\mathrm{MisREPA}(\hat{x})$$

$$\le \frac{4}{N}\sum_{n=1}^{N}\big\|f^{[n]}_{\mathrm{DINOv2}}(\bar{x}) - g_\phi(\textsc{DiffEnc}^{[n]}(\hat{x}))\big\|_2^2 + \frac{4}{N}\sum_{n=1}^{N}\big\|f^{[n]}_{\mathrm{DINOv2}}(x) - f^{[n]}_{\mathrm{DINOv2}}(\bar{x})\big\|_2^2 + 2\,\mathrm{MisREPA}(\hat{x}). \tag{8}$$

$$= \frac{4}{N}\sum_{n=1}^{N}\big\|f^{[n]}_{\mathrm{DINOv2}}(\bar{x}) - g_\phi(\textsc{DiffEnc}^{[n]}(\hat{x}))\big\|_2^2 + 4\mathrm{ApproxErr}(x,\bar{x}) + 2\mathrm{MisREPA}(\hat{x}). \tag{9}$$

Using the cosine–squared identity for unit–norm features,

$$\sum_{n=1}^{N} \big\| f_{\text{DINOv2}}^{[n]}(\bar{x}) - g_\phi(\text{DIFFENC}^{[n]}(\hat{x})) \big\|_2^2 = 2N\big(1 - \text{REPA}(\bar{x}, \hat{x})\big),$$

$$\big\|\mu_f(x) - \mu_f(\hat{x})\big\|_2^2 \;\le\; 8\Big(1 - \text{REPA}(\bar{x}, \hat{x})\Big) \;+\; 4\text{ApproxErr}(x, \bar{x}) \;+\; 2\,\text{MisREPA}(\hat{x}).$$

Rearranging gives the bound

$$\text{REPA}(\bar{x}, \hat{x}) \;\le\; 1 - \frac{1}{8}\big\|\mu_f(x) - \mu_f(\hat{x})\big\|_2^2 + \frac{1}{2}\,\text{ApproxErr}(x, \bar{x}) + \frac{1}{4}\,\text{MisREPA}(\hat{x}).$$

Taking expectations over $x \sim p_X$, and $\hat{x} \sim p_{\hat{X}}$, and using the convexity of the squared norm,

$$\mathbb{E}\big[\|\mu_f(x) - \mu_f(\hat{x})\|_2^2\big] \;\ge\; \big\|\mathbb{E}_x[\mu_f(x)] - \mathbb{E}_{\hat{x}}[\mu_f(\hat{x})]\big\|_2^2 = \text{MMD}_{\text{DINOv2}}(p_X, p_{\hat{X}}),$$

we obtain

$$\mathbb{E}_{\hat{x},\bar{x}}[\text{REPA}(\bar{x}, \hat{x})] \;\le\; 1 - \frac{1}{8}\,\text{MMD}_{\text{DINOv2}}\big(p_X,\, p_{\hat{X}}\big) + \frac{1}{2}\,\mathbb{E}_{x,\bar{x}}\big[\text{ApproxErr}(x, \bar{x})\big] + \frac{1}{4}\,\mathbb{E}_{\hat{x}}\big[\text{MisREPA}(\hat{x})\big], \tag{10}$$

Assumption A.2 (Regularity of the diffusion encoder and REPA projection)**.** We operate under the following regularity and conditioning assumptions on the diffusion feature extractor and the REPA projection. For notational simplicity in the analysis, we introduce an operator corresponding to the vectorized diffusion encoder. Let $\widetilde{G}(\cdot) := \text{vec}(\text{DIFFENC}(\cdot, t)) : \mathbb{R}^d \to \mathbb{R}^{ND}$ denote the vectorized diffusion feature extractor at timestep t, and let $\widetilde{g}_\phi : \mathbb{R}^{ND} \to \mathbb{R}^{ND}$ denote the patchwise lift of the projection head $g_\phi : \mathbb{R}^D \to \mathbb{R}^D$. Fix two diffusion states $z_t, z^* \in \mathbb{R}^d$ and define $u_t := \widetilde{G}(z_t)$ and $u^* := \widetilde{G}(z^*)$. Let

$$B := \{z^* + s(z_t - z^*) : s \in [0, 1]\} \quad \text{and} \quad \mathcal{U} := \{\widetilde{G}(z) : z \in B\}.$$

A.2.1 The mapping $\widetilde{G}$ is differentiable, and its Jacobian $J_{\widetilde{G}}(z) \in \mathbb{R}^{(ND)\times d}$ is Lipschitz continuous on B with Lipschitz constant L_G.

A.2.2 There exist constants $m_G > 0$ and $M_G < \infty$ such that

$$J_{\widetilde{G}}(z_t)^\top J_{\widetilde{G}}(z_t) \succeq m_G^2 I_d, \qquad \|J_{\widetilde{G}}(z)\|_2 \le M_G \quad \text{for all } z \in B.$$

A.2.3 The mapping $\widetilde{g}_\phi$ is differentiable, and its Jacobian $J_{\widetilde{g}_\phi}(u) \in \mathbb{R}^{(ND)\times(ND)}$ is uniformly well-conditioned at u_t: there exists a constant $m_\phi > 0$ such that

$$J_{\widetilde{g}_\phi}(u_t)^\top J_{\widetilde{g}_\phi}(u_t) \succeq m_\phi^2 I_{ND}, \qquad \|J_{\widetilde{g}_\phi}(u)\|_2 \le M_\phi \quad \text{for all } u \in \mathcal{U}.$$

A.2.4 The Jacobian $J_{\widetilde{g}_\phi}$ is Lipschitz continuous on $\mathcal{U}$ with Lipschitz constant L_ϕ.

Proposition A.3 (Local contraction of REPA in the diffusion state space)**.** *Consider an inverse problem in which an observation $y \in \mathbb{R}^m$ is generated from a ground-truth image $x \sim p_X$, and let $\bar{x} \sim p_{\bar{X}}$ denote the proxy approximation used during REPA. Let $z_t \in \mathbb{R}^d$ be the diffusion state at timestep t produced by Algorithm 1, and let $z_t^{(\text{REPA})}$ denote the diffusion state after applying the REPA regularization update. Let $z^* \in \mathbb{R}^d$ denote the latent variable associated with the clean image x. Under Assumptions A_1–A_4, define*

$$r := \frac{m_G^2\, m_\phi^2}{L_\phi M_G^3 M_\phi + L_G M_\phi^2 M_G.}$$

If $\|z_t - z^*\|_2 < r$, then there exists a stepsize

$$0 < \lambda \le \frac{1}{2M_G^2\, M_\phi^2}$$

such that the REPA update induces a local contraction in the diffusion state space. In particular,

$$\|z_t^{(\text{REPA})} - z^*\|_2 \;\le\; C_1\,\|z_t - z^*\|_2 + C_2\left(\sqrt{\text{ApproxErr}(x, \bar{x})} + \sqrt{\text{MisREPA}(x)}\right),$$

where

$$C_1 := 1 - \lambda m_G^2 m_\phi^2 \in (0, 1), \qquad C_2 := 2\,\lambda\, M_G\, M_\phi \sqrt{N}.$$

Proof. We first rewrite all quantities in vectorized form. Let $\mathrm{vec}(\cdot)$ denote the operator that stacks the rows of a matrix into a single vector. For any matrix $H \in \mathbb{R}^{k_1 \times k_2}$, define

$$\widetilde{H} := \mathrm{vec}(H) \in \mathbb{R}^{k_1 k_2}.$$

For the DINOv2 features $f_{\mathrm{DINOv2}}(x) \in \mathbb{R}^{N \times D}$ we write

$$\widetilde{f}(x) := \mathrm{vec}\big(f_{\mathrm{DINOv2}}(x)\big) \in \mathbb{R}^{ND}.$$

For the diffusion-model feature extractor $\textsc{DiffEnc} : \mathbb{R}^d \times \mathbb{R} \to \mathbb{R}^{N \times D}$, we define its vectorized form by

$$\widetilde{G}(z_t) := \mathrm{vec}\big(\textsc{DiffEnc}(z_t, t)\big) \in \mathbb{R}^{ND}.$$

Recall that $\phi : \mathbb{R}^D \to \mathbb{R}^D$ is differentiable. Its lifted Jacobian acts patchwise and satisfies

$$J_{\widetilde{g}_\phi}(\widetilde{G}(z_t)) = I_N \otimes J_\phi(G_2(z_t)).$$

The REPA update is given by

$$z_t^{(\mathrm{REPA})} = z_t - \lambda \nabla_{z_t} \big\| \widetilde{f}(\bar{x}) - \widetilde{g}_\phi(\widetilde{G}(z_t)) \big\|_2^2.$$

By the chain rule,

$$z_t^{(\mathrm{REPA})} = z_t + 2\lambda\, J_{\widetilde{G}}(z_t)^\top J_{\widetilde{g}_\phi}(\widetilde{G}(z_t))^\top \big(\widetilde{f}(\bar{x}) - \widetilde{g}_\phi(\widetilde{G}(z_t))\big).$$

Subtracting z^* from both sides yields

$$z_t^{(\mathrm{REPA})} - z^* = z_t - z^* + 2\lambda\, J_{\widetilde{G}}(z_t)^\top J_{\widetilde{g}_\phi}(\widetilde{G}(z_t))^\top \big(\widetilde{f}(\bar{x}) - \widetilde{g}_\phi(\widetilde{G}(z_t))\big).$$

We now add and subtract $\widetilde{f}(x)$ and $\widetilde{g}_\phi(\widetilde{G}(z^*))$ inside the parentheses:

$$\begin{aligned} z_t^{(\mathrm{REPA})} - z^* = (z_t - z^*) &- 2\lambda\, J_{\widetilde{G}}(z_t)^\top J_{\widetilde{g}_\phi}(\widetilde{G}(z_t))^\top \big(\widetilde{g}_\phi(\widetilde{G}(z_t)) - \widetilde{g}_\phi(\widetilde{G}(z^*))\big) \\ &+ 2\lambda\, J_{\widetilde{G}}(z_t)^\top J_{\widetilde{g}_\phi}(\widetilde{G}(z_t))^\top \big(\widetilde{f}(\bar{x}) - \widetilde{f}(x)\big) \\ &+ 2\lambda\, J_{\widetilde{G}}(z_t)^\top J_{\widetilde{g}_\phi}(\widetilde{G}(z_t))^\top \big(\widetilde{f}(x) - \widetilde{g}_\phi(\widetilde{G}(z^*))\big). \end{aligned} \tag{11}$$

We define the *contractive part* as

$$\mathcal{T}_t := (z_t - z^*) - 2\lambda\, J_{\widetilde{G}}(z_t)^\top J_{\widetilde{g}_\phi}(\widetilde{G}(z_t))^\top \big(\widetilde{g}_\phi(\widetilde{G}(z_t)) - \widetilde{g}_\phi(\widetilde{G}(z^*))\big).$$

Applying the fundamental theorem of calculus to $u \mapsto \widetilde{g}_\phi(u)$ along $u(s) = \widetilde{G}(z(s))$ with $z(s) = z^* + s(z_t - z^*)$, $s \in [0,1]$, yields

$$\widetilde{g}_\phi(\widetilde{G}(z_t)) - \widetilde{g}_\phi(\widetilde{G}(z^*)) = \int_0^1 J_{\widetilde{g}_\phi}\big(\widetilde{G}(z(s))\big)\, J_{\widetilde{G}}\big(z(s)\big)\, (z_t - z^*)\, ds.$$

Substituting into the definition of $\mathcal{T}_t$ gives

$$\mathcal{T}_t = \Big[I - 2\lambda \int_0^1 J_{\widetilde{G}}(z_t)^\top J_{\widetilde{g}_\phi}\big(\widetilde{G}(z_t)\big)^\top J_{\widetilde{g}_\phi}\big(\widetilde{G}(z(s))\big) J_{\widetilde{G}}\big(z(s)\big)\, ds\Big](z_t - z^*). \tag{12}$$

Add and subtract $J_{\widetilde{g}_\phi}(\widetilde{G}(z_t))\, J_{\widetilde{G}}(z_t)$ inside the integral to obtain

$$\begin{aligned} \mathcal{T}_t = &\Big[I - 2\lambda\, J_{\widetilde{G}}(z_t)^\top J_{\widetilde{g}_\phi}(\widetilde{G}(z_t))^\top J_{\widetilde{g}_\phi}(\widetilde{G}(z_t)) J_{\widetilde{G}}(z_t)\Big](z_t - z^*) \\ &- 2\lambda\Big[\int_0^1 J_{\widetilde{G}}(z_t)^\top J_{\widetilde{g}_\phi}(\widetilde{G}(z_t))^\top \Big(J_{\widetilde{g}_\phi}(\widetilde{G}(z(s)))\, J_{\widetilde{G}}(z(s)) - J_{\widetilde{g}_\phi}(\widetilde{G}(z_t))\, J_{\widetilde{G}}(z_t)\Big)\, ds\Big](z_t - z^*). \end{aligned} \tag{13}$$

Taking Euclidean norms in (13) and using the triangle inequality gives

$$\begin{aligned} \|\mathcal{T}_t\|_2 \le &\Big\|I - 2\lambda\, J_{\widetilde{G}}(z_t)^\top J_{\widetilde{g}_\phi}(\widetilde{G}(z_t))^\top J_{\widetilde{g}_\phi}(\widetilde{G}(z_t)) J_{\widetilde{G}}(z_t)\Big\|_2\, \|z_t - z^*\|_2 \\ &+ 2\lambda \Big\|\int_0^1 J_{\widetilde{G}}(z_t)^\top J_{\widetilde{g}_\phi}(\widetilde{G}(z_t))^\top \Big(J_{\widetilde{g}_\phi}(\widetilde{G}(z(s)))\, J_{\widetilde{G}}(z(s)) - J_{\widetilde{g}_\phi}(\widetilde{G}(z_t))\, J_{\widetilde{G}}(z_t)\Big)\, ds\Big\|_2\, \|z_t - z^*\|_2. \end{aligned} \tag{14}$$

Moreover, by submultiplicativity of the spectral norm and $\left\|\int_0^1 A(s)\,ds\right\|_2 \le \int_0^1 \|A(s)\|_2\,ds$, the second term can be bounded as

$$\Big\| \int_0^1 J_{\widetilde{G}}(z_t)^\top J_{\widetilde{g}_\phi}(\widetilde{G}(z_t))^\top \Big(J_{\widetilde{g}_\phi}(\widetilde{G}(z(s)))\, J_{\widetilde{G}}(z(s)) - J_{\widetilde{g}_\phi}(\widetilde{G}(z_t))\, J_{\widetilde{G}}(z_t) \Big)\, ds \Big\|_2 \le \tag{15}$$

$$\int_0^1 \|J_{\widetilde{G}}(z_t)\|_2\, \|J_{\widetilde{g}_\phi}(\widetilde{G}(z_t))\|_2 \Big\| J_{\widetilde{g}_\phi}(\widetilde{G}(z(s)))\, J_{\widetilde{G}}(z(s)) - J_{\widetilde{g}_\phi}(\widetilde{G}(z_t))\, J_{\widetilde{G}}(z_t) \Big\|_2 \, ds. \tag{16}$$

Combining (14)–(16) yields

$$\begin{aligned}\|\mathcal{T}_t\|_2 \le{}& \Big\| I - 2\lambda\, J_{\widetilde{G}}(z_t)^\top J_{\widetilde{g}_\phi}(\widetilde{G}(z_t))^\top J_{\widetilde{g}_\phi}(\widetilde{G}(z_t)) J_{\widetilde{G}}(z_t) \Big\|_2\, \|z_t - z^*\|_2 \\ &+ 2\lambda \Big(\int_0^1 \|J_{\widetilde{G}}(z_t)\|_2\, \|J_{\widetilde{g}_\phi}(\widetilde{G}(z_t))\|_2 \Big\| J_{\widetilde{g}_\phi}(\widetilde{G}(z(s)))\, J_{\widetilde{G}}(z(s)) - J_{\widetilde{g}_\phi}(\widetilde{G}(z_t))\, J_{\widetilde{G}}(z_t) \Big\|_2 \, ds \Big) \|z_t - z^*\|_2.\end{aligned} \tag{17}$$

We bound the difference inside the integral by writing

$$\begin{aligned}&\Big\| J_{\widetilde{g}_\phi}(\widetilde{G}(z(s)))\, J_{\widetilde{G}}(z(s)) - J_{\widetilde{g}_\phi}(\widetilde{G}(z_t))\, J_{\widetilde{G}}(z_t) \Big\|_2 \\ &\le \Big\| \big(J_{\widetilde{g}_\phi}(\widetilde{G}(z(s))) - J_{\widetilde{g}_\phi}(\widetilde{G}(z_t)) \big) J_{\widetilde{G}}(z(s)) \Big\|_2 + \Big\| J_{\widetilde{g}_\phi}(\widetilde{G}(z_t)) \big(J_{\widetilde{G}}(z(s)) - J_{\widetilde{G}}(z_t) \big) \Big\|_2 \\ &\le \|J_{\widetilde{g}_\phi}(\widetilde{G}(z(s))) - J_{\widetilde{g}_\phi}(\widetilde{G}(z_t))\|_2\, \|J_{\widetilde{G}}(z(s))\|_2 + \|J_{\widetilde{g}_\phi}(\widetilde{G}(z_t))\|_2\, \|J_{\widetilde{G}}(z(s)) - J_{\widetilde{G}}(z_t)\|_2.\end{aligned} \tag{18}$$

Using the Lipschitz property of $J_{\widetilde{G}}$,

$$\|J_{\widetilde{G}}(z(s)) - J_{\widetilde{G}}(z_t)\|_2 \le L_G\, \|z(s) - z_t\|_2 = L_G(1-s)\, \|z_t - z^*\|_2,$$

together with the Lipschitz continuity of $J_{\widetilde{g}_\phi}$,

$$\|J_{\widetilde{g}_\phi}(\widetilde{G}(z(s))) - J_{\widetilde{g}_\phi}(\widetilde{G}(z_t))\|_2 \le L_\phi M_G (1-s)\, \|z_t - z^*\|_2,$$

and the uniform bounds

$$\|J_{\widetilde{G}}(z(s))\|_2 \le M_G, \qquad \|J_{\widetilde{g}_\phi}(\widetilde{G}(z_t))\|_2 \le M_\phi,$$

This yields

$$\Big\| J_{\widetilde{g}_\phi}(\widetilde{G}(z(s)))\, J_{\widetilde{G}}(z(s)) - J_{\widetilde{g}_\phi}(\widetilde{G}(z_t))\, J_{\widetilde{G}}(z_t) \Big\|_2 \le (1-s) \Big(L_\phi M_G^2 + L_G M_\phi \Big) \|z_t - z^*\|_2.$$

Substituting this bound into (17) and integrating over $s \in [0,1]$ yields

$$\begin{aligned}\|\mathcal{T}_t\|_2 \le{}& \Big\| I - 2\lambda\, J_{\widetilde{G}}(z_t)^\top J_{\widetilde{g}_\phi}(\widetilde{G}(z_t))^\top J_{\widetilde{g}_\phi}(\widetilde{G}(z_t)) J_{\widetilde{G}}(z_t) \Big\|_2\, \|z_t - z^*\|_2 \\ &+ \lambda \Big(L_\phi M_G^3 M_\phi + L_G M_\phi^2 M_G \Big) \|z_t - z^*\|_2^2.\end{aligned} \tag{19}$$

Since the symmetric matrix

$$S_t := J_{\widetilde{G}}(z_t)^\top J_{\widetilde{g}_\phi}(\widetilde{G}(z_t))^\top J_{\widetilde{g}_\phi}(\widetilde{G}(z_t)) J_{\widetilde{G}}(z_t)$$

has eigenvalues contained in $[m_G^2 m_\phi^2,\ M_G^2 M_\phi^2]$, its spectral norm satisfies

$$\big\| I - 2\lambda S_t \big\|_2 = \max_{\sigma \in [m_G^2 m_\phi^2,\, M_G^2 M_\phi^2]} |1 - 2\lambda\sigma|.$$

For any $0 < \lambda \le 1/(2M_G^2 M_\phi^2)$, the maximum is attained at $\sigma = m_G^2 m_\phi^2$, and hence

$$\big\| I - 2\lambda S_t \big\|_2 \le 1 - 2\lambda m_G^2 m_\phi^2.$$

Substituting this bound into (19) yields

$$\|\mathcal{T}_t\|_2 \le \Big(1 - 2\lambda m_G^2 m_\phi^2 + \lambda \Big(L_\phi M_G^3 M_\phi + L_G M_\phi^2 M_G \Big) \|z_t - z^*\|_2 \Big) \|z_t - z^*\|_2. \tag{20}$$

Therefore, if

$$\|z_t - z^*\|_2 < \frac{m_G^2\, m_\phi^2}{L_\phi M_G^3 M_\phi + L_G M_\phi^2 M_G} \qquad \text{and} \qquad 0 < \lambda \le \frac{1}{2M_G^2 M_\phi^2},$$

then the contractive part satisfies the strict contraction

$$\|\mathcal{T}_t\|_2 \le \left(1 - \lambda m_G^2 m_\phi^2\right) \|z_t - z^*\|_2,$$

with contraction factor strictly smaller than one. By the definitions of the approximation and misalignment errors,

$$\|\widetilde{f}(\bar{x}) - \widetilde{f}(x)\|_2 = \sqrt{N}\,\sqrt{\mathrm{ApproxErr}(x,\bar{x})}, \qquad \|\widetilde{f}(x) - \widetilde{g}_\phi\left(\widetilde{G}(z^*)\right)\|_2 = \sqrt{N}\,\sqrt{\mathrm{MisREPA}(x)}.$$

Returning to the decomposition we combine the contraction bound for $\mathcal{T}_t$ with the remaining two terms. Using the triangle inequality together with the uniform bounds $\|J_{\widetilde{G}}(z_t)\|_2 \le M_G$ and $\|J_{\widetilde{g}_\phi}(\widetilde{G}(z_t))\|_2 \le M_\phi$, we obtain

$$\begin{aligned}\|z_t^{(\mathrm{repa})} - z^*\|_2 \le \|\mathcal{T}_t\|_2 &+ 2\lambda M_G M_\phi\, \|\widetilde{f}(\bar{x}) - \widetilde{f}(x)\|_2 \\ &+ 2\lambda M_G M_\phi\, \|\widetilde{f}(x) - \widetilde{g}_\phi(\,\widetilde{G}(z^*))\|_2. \end{aligned} \tag{21}$$

Substituting the contraction estimate together with the above identities yields

$$\|z_t^{(\mathrm{REPA})} - z^*\|_2 \le (1 - \lambda m_G^2 m_\phi^2)\, \|z_t - z^*\|_2 + C\Big(\sqrt{\mathrm{ApproxErr}(x,\bar{x})} + \sqrt{\mathrm{MisREPA}(x)}\Big), \tag{22}$$

where the constant C is defined explicitly as

$$C := 2\lambda M_G M_\phi \sqrt{N}.$$

This concludes the proof.

A.2 Details About Latent DPS + REPA Implementation

We implement Latent DPS + REPA following Algorithm 2 and use 1000 sampling steps throughout. We employ an SNR-based learning rate schedule of the form

$$\eta(t) = \frac{\kappa}{\max\left(\frac{t}{1-t},\, 1\right)},$$

where κ is a tunable scaling factor. This schedule accounts for the varying signal-to-noise ratio across diffusion timesteps and provides stable performance in practice. The parameters κ and the representation-alignment strength λ are tuned on a small validation set with present the best parameters found in Table 2.

Table 2: Hyperparameters used for Latent DPS + REPA.

	ImageNet		**FFHQ**	
Task	$\boldsymbol{\kappa}$	$\boldsymbol{\lambda}$	$\boldsymbol{\kappa}$	$\boldsymbol{\lambda}$
Super-resolution	2.0	0.01	*1.25*	*0.025*
Gaussian deblurring	0.25	0.05	*0.5*	*0.05*
Motion deblurring	0.5	0.01	*0.5*	*0.05*
Box inpainting	0.5	0.01	*0.75*	*0.025*

A.3 Details About Resample + REPA Implementation

In Table 3, we present an adaptation of the algorithm proposed in [32] to the flow-based setting, augmented with the REPA regularizer as described in the methodology section. We note that the original ReSample algorithm employs a three-stage procedure for enforcing data consistency: (i) gradient steps in latent space, similar to Latent DPS; (ii) pixel-space optimization, which is

Algorithm 2 Latent DPS + REPA Algorithm

Require: flow model u_θ, measurement y, pretrained encoder f, proxy representation c_{proxy}, timestep t_{cutoff}, initialize $z_T \sim \mathcal{N}(0, I)$

1: **for** $t \in \{T, \dots, 0\}$ **do**
2: $\quad v \leftarrow u_\theta(z_t, t)$
3: $\quad \hat{z}_0 \leftarrow \mathbb{E}[z_0 \mid z_t]$
4: $\quad z_{t-1} \leftarrow z_t - \frac{1}{T} \cdot v$
5: $\quad z_{t-1} \leftarrow z_{t-1} - \eta \nabla_{z_t} \|y - \mathcal{A}(\mathcal{D}(\hat{z}_0))\|_2^2$
6: $\quad z_{t-1} \leftarrow z_{t-1} + \lambda \nabla_{z_t} \sum_{n=1}^{N} \cos(c_{\text{proxy}}^{[n]}, g_\phi(\text{DiffEnc}^{[n]}(z_t, t))$
7: $\quad$ **if** $t < t_{\text{cutoff}}$ **then**
8: $\quad\quad c_{\text{proxy}} \leftarrow f_{\text{DINOv2}}\big(\mathcal{D}(\mathbb{E}[z_0 \mid z_t])\big)$
9: $\quad$ **end if**
10: **end for**
11: **return** x_0

Table 3: Hyperparameters used for Resampling + REPA.

	ImageNet				FFHQ			
Task	κ	λ	**max iters**	**inner lr**	κ	λ	**max iters**	**inner lr**
Super-resolution	0.05	3.25	150	0.005	0.01	2.25	100	0.0001
Gaussian deblurring	0.075	0.5	300	0.005	0.05	0.75	300	0.00075
Motion deblurring	0.5	0.75	300	0.005	0.05	0.75	100	0.005
Box inpainting	0.025	100	200	0.0005	0.05	0.75	200	0.0005

computationally efficient and captures high-level semantics but often leads to blurrier reconstructions; and (iii) latent space optimization as outlined to line 7 of Algorithm 3. In contrast, our adaptation omits the pixel-space stage, as our focus is on maximizing perceptual quality. We found that this modification together with the inclusion of the REPA reguralizer yields sharper and more visually convincing results, while still benefiting from the refinement effect of the final latent-space consistency updates. The best hyperparameters used for this variant are reported in Table 3. In addition to the parameters κ and λ, which play analogous roles to those in Latent DPS, we also tune the maximum number of inner-loop optimization steps and the corresponding inner learning rate of the Resample procedure (see Algorithm 3).

A.4 Robustness of DINOv2 Representations to Corruptions

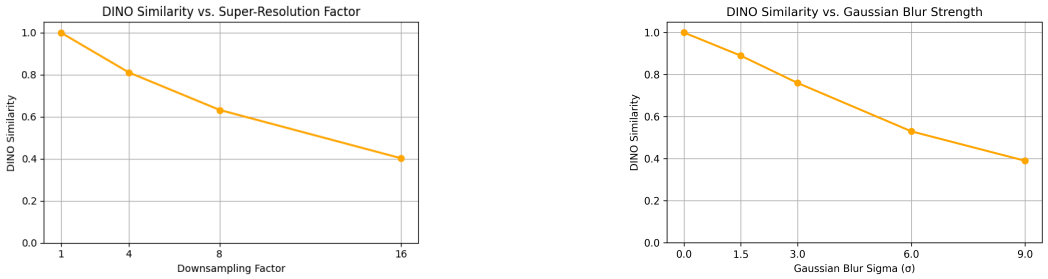
To evaluate the robustness of DINOv2 representations under various corruptions, we conduct experiments on a fixed set of 100 images on the ImageNet dataset (Similar results hold for the FFHQ dataset as illustrated in Appendix A.6). For each image, we compute the average patch similarity between its ground truth representation and that of its corrupted version. We assess this similarity across different corruption types specifically super-resolution and Gaussian deblurring at varying levels of severity. We report the average similarity across the selected subset of 100 images.

Figure 5 first visualizes how the pixel-space appearance of a single image changes across different corruption levels. Figure 4 then shows how the DINOv2 representation similarity changes as the corruption severity increases for the two tasks. Interestingly, we observe that DINOv2 representations remain significantly more robust to both super-resolution and Gaussian deblurring. Despite substantial visual degradation in pixel space, DINOv2 features maintain a strong alignment with the original image features.

Algorithm 3 Resample + REPA Algorithm

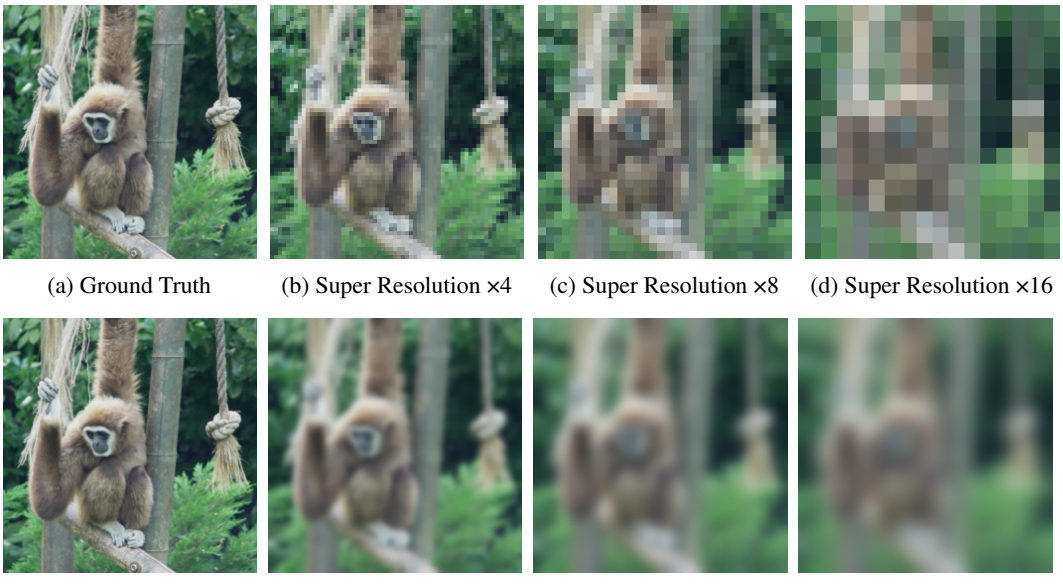
Require: flow model u_θ, measurement y, pretrained encoder f, resample steps C, parameter γ, proxy representation c_{proxy}, timestep t_{cutoff}, initialize $z_T \sim \mathcal{N}(0, I)$

for $t \in \{T, \dots, 0\}$ **do**
  $\hat{z}_0 \leftarrow \mathbb{E}[z_0 \mid z_t]$
  $z_{t-1} \leftarrow z_t - \frac{1}{T} \cdot u_\theta(z_t, t)$
  if $t \in C$ **then**
    $\tilde{z}_0(y) \leftarrow \arg\min_z \frac{1}{2}\|y - \mathcal{A}(\mathcal{D}(z))\|_2^2$ ▷ initialize at $\hat{z}_0$
    $z_{t-1} \leftarrow \textsc{StochasticResample}(\tilde{z}_0(y),\, z_{t-1},\, \gamma)$
  end if
  $z_{t-1} \leftarrow z_{t-1} + \lambda \nabla_{z_t} \sum_{n=1}^{N} \cos\big(c_{\text{proxy}}^{[n]},\, g_\phi(\text{DiffEnc}^{[n]}(z_t, t))\big)$
  if $t < t_{\text{cutoff}}$ **then**
    $c_{\text{proxy}} \leftarrow f_{\text{DINOv2}}\big(\mathcal{D}(\mathbb{E}[z_0 \mid z_t])\big)$
  end if
end for
$x_0 \leftarrow \mathcal{D}(z_0)$
return x_0



(a) Super-Resolution (b) Gaussian Deblurring

Figure 4: Similarity of representations under increasing levels of corruption.



(a) Ground Truth (b) Super Resolution ×4 (c) Super Resolution ×8 (d) Super Resolution ×16

(e) Ground Truth (f) Gaussian deblur $\sigma = 3$ (g) Gaussian deblur $\sigma = 6$ (h) Gaussian deblur $\sigma = 9$

Figure 5: Visual comparison of a corrupted images for different corruption types and severity levels.

A.5 Selection of Proxy Representation

Since pretrained DINOv2 features are robust to a wide range of common image corruptions, we use the DINOv2 encoding of the measurement as an initial proxy representation, $f_{\mathrm{DINOv2}}(y)$. We find this choice to be effective across all considered inverse problems. In addition, we introduce a cutoff timestep at which the proxy representation is updated to depend on the model's current denoised estimate, namely $f_{\mathrm{DINOv2}}(\mathcal{D}(\mathbb{E}[z_0 \mid z_t]))$.

- **Box Inpainting.** We construct the proxy representation by combining the observed regions of the measurement with the model's current denoised estimate:

$$c_{\text{proxy}} = \mathrm{mask} \odot f_{\mathrm{DINOv2}}(y) + (I - \mathrm{mask}) \odot f_{\mathrm{DINOv2}}\big(\mathcal{D}(\mathbb{E}[z_0 \mid z_t])\big), \tag{23}$$

  where mask denotes the binary inpainting mask.
- **Super-resolution, Gaussian Deblurring, and Motion Deblurring.** For these tasks, we use $f_{\mathrm{DINOv2}}(y)$ as the proxy representation during the early stages of sampling. On the FFHQ dataset, we find it beneficial to switch to the reconstruction-based proxy $f_{\mathrm{DINOv2}}(\mathcal{D}(\mathbb{E}[z_0 \mid z_t]))$ after 80% of the diffusion steps. On ImageNet, this transition does not lead to consistent improvements, and we therefore use the measurement-based proxy throughout. We include an ablation to justify these choices in A.10.

A.6 Results Using a CLIP Model

In this subsection, we compare the results obtained using a DINOv2 encoder with those obtained using a CLIP model. To this end, we train a model with representation alignment using CLIP representations instead of DINOv2 representations on the FFHQ dataset. Both models were trained for 100K iterations using a batch size of 256. Table 4 presents quantitative results when applying our inference-time framework to both models. As we can see, the inclusion of our regularizer leads to consistent improvements across all tasks and metrics.

To compare the influence of DINOv2 and CLIP, we make the following observations. First, the baseline algorithm performs slightly better when the model has been trained using DINOv2 representations rather than CLIP. This result is consistent with the findings of [42], where the best-performing model was also trained using DINOv2 representations, suggesting that DINOv2-based representation alignment leads to a stronger generative prior. Regarding the comparison of our test-time regularizer between DINOv2 and CLIP, we observe that DINOv2 representations appear to be more robust to the standard degradations used in inverse problem evaluation. We illustrate this behavior in Figure 6.

Table 4: Performance comparison on FFHQ ($\sigma = 0.05$) for models trained with DINOv2 and CLIP representations.

Task	Method	LPIPS↓	FID↓	PSNR↑	SSIM↑
$4\times$ SR	Latent DPS (DINOv2-trained)	0.188	56.69	28.99	0.814
	Latent DPS + REPA (DINOv2-trained)	**0.176**	**51.27**	**29.12**	**0.819**
	Latent DPS (CLIP-trained)	0.190	63.63	28.95	0.811
	Latent DPS + REPA (CLIP-trained)	0.183	54.88	28.99	0.815
Box Inpainting	Latent DPS (DINOv2 Trained)	0.192	65.89	23.55	**0.785**
	Latent DPS + REPA (DINOv2 Trained)	**0.178**	**57.04**	**23.83**	0.784
	Latent DPS (CLIP-trained)	0.193	54.01	23.53	0.784
	Latent DPS + REPA (CLIP-trained)	0.185	52.45	23.65	0.784
Gaussian Deblur	Latent DPS (DINOv2-trained)	0.192	60.65	28.15	0.783
	Latent DPS + REPA (DINOv2-trained)	**0.186**	**55.53**	**28.21**	**0.787**
	Latent DPS (CLIP-trained)	0.193	60.72	28.02	0.782
	Latent DPS + REPA (CLIP-trained)	0.188	59.76	28.07	0.779

A.7 Solving Inverse Problems under Severe Degradations

In this subsection, we study the effect of the REPA regularizer under severe degradations. We evaluate the performance of our method using Latent DPS on the FFHQ dataset for both super-resolution and

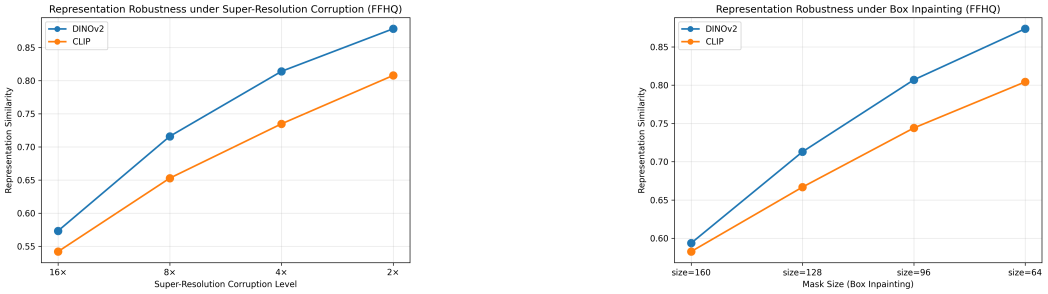
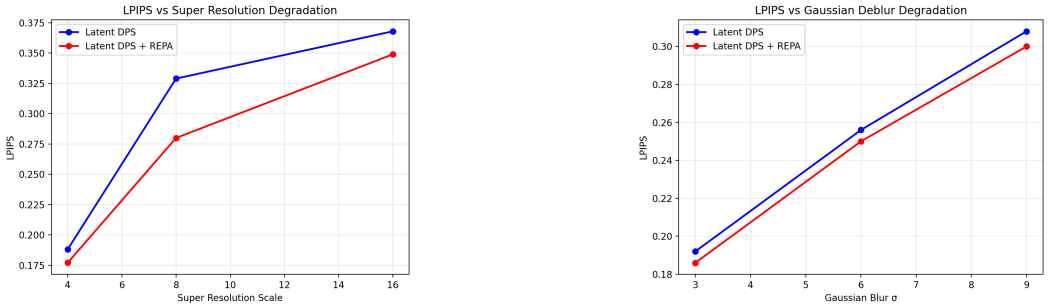


Figure 6: Comparison of the DINOv2 and CLIP robustness to common degradations.

Table 5: Performance under severe degradations on FFHQ using Latent DPS.

Task	**Method**	LPIPS↓	FID↓	PSNR↑	SSIM↑
8× Super Resolution	Latent DPS	0.329	92.18	22.85	0.593
	Latent DPS + REPA	0.280	72.70	23.24	0.617
16× Super Resolution	Latent DPS	0.368	109.87	20.11	0.499
	Latent DPS + REPA	0.349	95.87	20.41	0.523
Gaussian Deblur ($\sigma = 6$)	Latent DPS	0.256	77.82	24.35	0.658
	Latent DPS + REPA	0.250	72.43	24.42	0.665
Gaussian Deblur ($\sigma = 9$)	Latent DPS	0.308	86.58	21.82	0.566
	Latent DPS + REPA	0.300	81.84	21.97	0.582

Gaussian deblurring. For super-resolution, we consider more challenging settings with $8\times$ and $16\times$ upscaling factors, while for Gaussian deblurring we consider stronger blur levels with $\sigma = 6$ and $\sigma = 9$. Figure 7 shows how LPIPS varies as the degradation severity increases. We also include the full quantitative results in Table 5.



LPIPS vs Super Resolution Degradation LPIPS vs Gaussian Deblur Degradation

Figure 7: LPIPS as a function of degradation severity for super-resolution (left) and Gaussian deblurring (right). REPA consistently improves perceptual quality across all degradation levels.

A.8 Extension to Non Linear Problems

In this section, we extend our evaluation of the REPA regularizer to more complex inverse problems. Specifically, we evaluate our method on non-linear deblurring and high dynamic range reconstruction using the degradation model of [43]. Table 6 presents quantitative results for Latent DPS and Resample, indicating improved performance when incorporating the REPA regularizer.

Table 6: Performance comparison on ImageNet for non-linear degradation tasks.

Task	Method	ImageNet LPIPS↓	FID↓	PSNR↑	SSIM↑
Non-linear Deblurring	Latent DPS	0.302	170.41	24.62	0.653
	Latent DPS + REPA	0.266	105.73	24.52	0.645
	Resample	0.276	141.44	25.04	0.661
	Resample + REPA	**0.248**	**103.96**	**25.13**	**0.668**
HDR Reconstruction	Latent DPS	0.310	138.78	23.12	0.690
	Latent DPS + REPA	**0.258**	**78.24**	**24.11**	0.701
	Resample	0.295	125.00	23.61	0.701
	Resample + REPA	0.282	108.41	24.01	**0.711**

A.9 Effect of the Choice of Transformer Block for Representation Alignment

We include an ablation study investigating the transformer block at which representation alignment is applied. We use the ImageNet model from [42] and study the effect of changing the alignment layer for the task of $4\times$ super-resolution. The mapping g_ϕ for the ImageNet model was trained using representations from the eighth transformer block. Figure 8 shows how performance varies when alignment is applied at different transformer blocks. The reported LPIPS values are averaged over 50 images. We observe that applying alignment at different blocks still leads to performance improvements; however, the largest improvements are obtained when alignment is applied at the same block on which the mapping g_ϕ was trained.

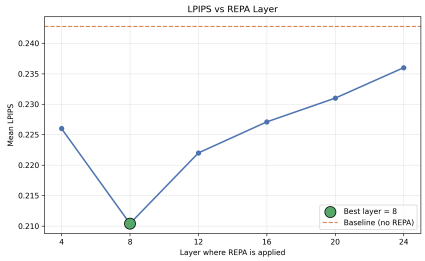


Figure 8: Ablation study on the transformer block used for representation alignment.

A.10 Ablation Studies

In this subsection, we present ablation studies on the main hyperparameters of our framework. The hyperparameters were selected through a small grid search on a validation set of 15 images. The results are summarized in Figure 9. Each row corresponds to a different task and dataset, while the columns correspond to the hyperparameters t_{cutoff}, the regularization strength λ, and the learning rate k. For each hyperparameter, we report the best LPIPS value obtained when fixing that parameter and varying the remaining hyperparameters.

Regarding the selection of the cutoff timestep, we observe that switching to the denoised estimate at very early timesteps leads to significantly worse performance compared to switching later in the diffusion process. This can be explained by the fact that the denoised estimate is still very noisy during the early diffusion steps. Our framework leverages the robustness of the DINOv2 features and therefore benefits from using the denoised estimate only after a sufficiently large cutoff timestep. Interestingly, for ImageNet we found that the best performance is obtained without switching, indicating that the optimal cutoff strategy depends on the dataset and reconstruction difficulty.

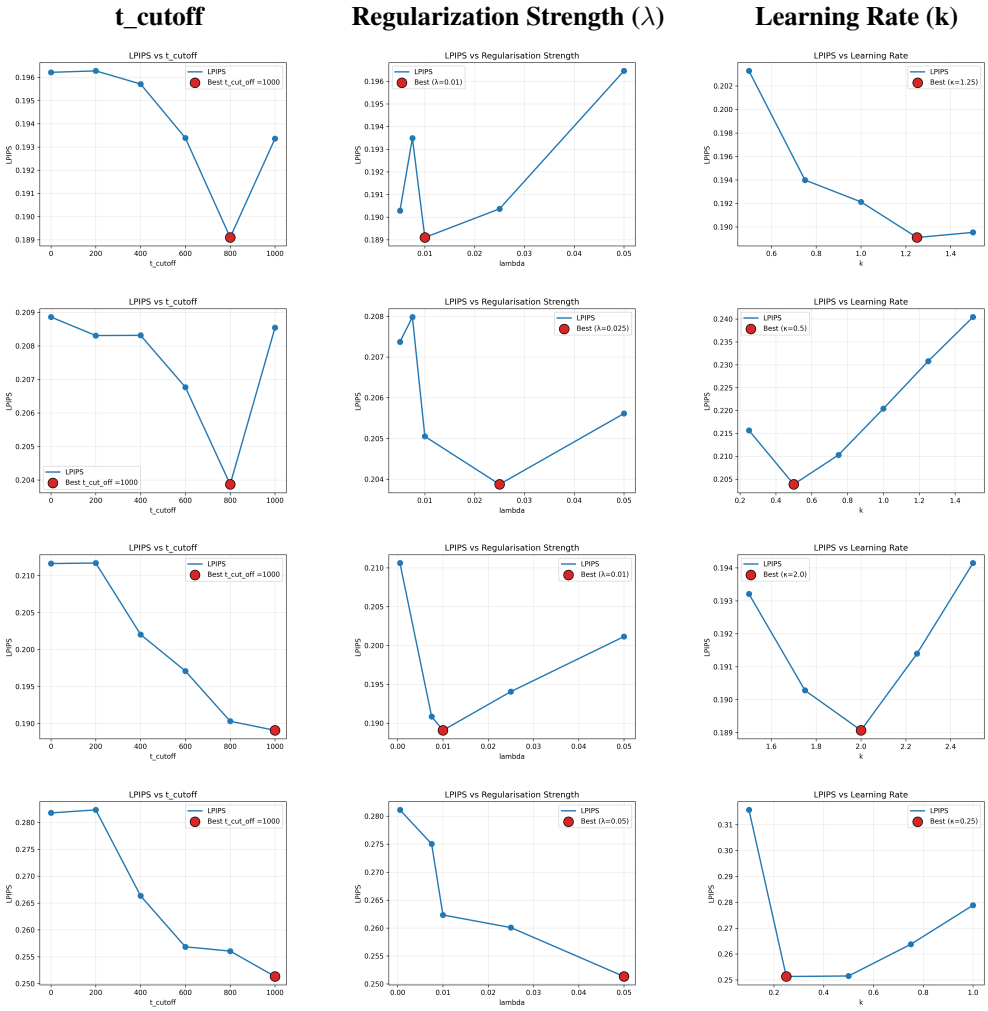


Figure 9: Ablation studies on the main hyperparameters of our framework. Rows correspond to different tasks and datasets: the first row shows FFHQ super-resolution, the second row FFHQ Gaussian deblurring, the third row ImageNet super-resolution, and the fourth row ImageNet Gaussian deblurring. Each plot shows the best LPIPS value achievable when the corresponding hyperparameter is fixed and the remaining hyperparameters are varied.

A.11 Experimental Details

We implement the inverse problem operators following the setup of [5]. For deblurring tasks, we follow [43] and fix a single realization of the degradation operator to ensure fair and consistent comparisons across methods. All baseline results are obtained using the official implementations provided by [5] and [43].

For DPS, we use the dataset-specific hyperparameters reported in the original paper. For DAPS, we adopt the hyperparameters provided in the official codebase for latent diffusion models.

For PSNR and SSIM, we report results obtained by averaging the reconstructed images across five independent runs of the solver and then computing the metrics on the averaged reconstruction.

A.12 Perception Distortion Tradeoff

We include qualitative examples for the task of $4\times$ super-resolution on the ImageNet dataset. In these examples, we observe that although the reconstructions obtained with REPA are perceptually more realistic and contain sharper details, the PSNR values do not necessarily increase. More generally, we

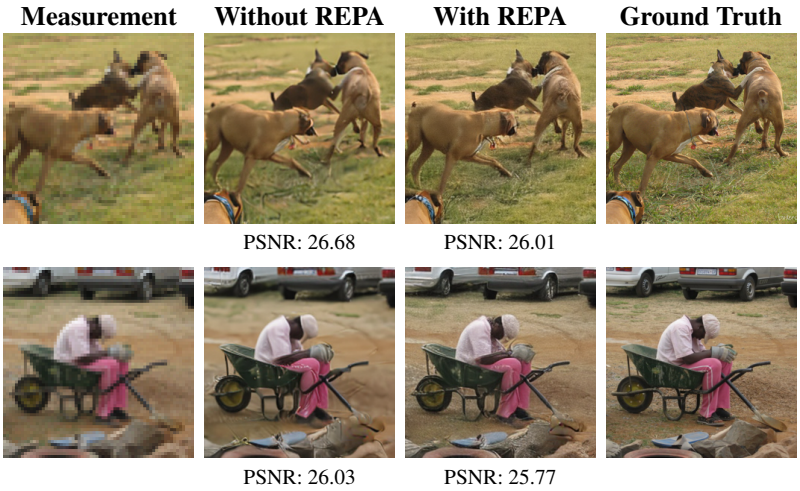


Figure 10: Qualitative comparison for $4\times$ super-resolution on the ImageNet dataset. While REPA produces sharper and more perceptually realistic reconstructions, these do not necessarily correspond to higher PSNR values, illustrating the perception–distortion trade-off.

observe that PSNR often favours smoother images, whereas perceptual metrics and visual inspection favour images with sharper details.

A.13 Enforcing Feature-Level DINOv2 Consistency without Representation Alignment

In this ablation study, we compare REPA against a variant that enforces consistency directly in the DINOv2 feature-space, without involving the diffusion model representations. More specifically, instead of using the representation alignment loss in line 8 of Algorithm 2, we replace it with the following update step:

$$z_{t-1} \leftarrow z_{t-1} + \lambda \nabla_{z_t} \sum_{n=1}^{N} \cos\Big(c_{\text{proxy}}^{[n]},\ f_{\text{DINOv2}}^{[n]}\big(\mathcal{D}(\mathbb{E}[z_0 \mid z_t])\big)\Big)\,, \tag{24}$$

Note that in this case we can only use $f_{\text{DINOv2}}(y)$ as the proxy term. While both objectives influence the sampling trajectory, the feature-only variant derives its guidance from the DINOv2 features of the decoded image. In contrast, REPA aligns the diffusion model's internal representations with DINOv2 features directly at each timestep. As shown in Table 7, the direct feature-space alignment yields consistently lower perceptual quality than the proposed representation-based formulation. for both experiments we have chosen the best hyperparameters using a small grid search as in A.2 to ensure fairness in comparison.

Table 7: Quantitative comparison between REPA and direct feature-space alignment.

Method	Super-resolution ($\times 4$) LPIPS ↓	FID ↓	Gaussian deblurring LPIPS ↓	FID ↓
Feature-space alignment	0.227	95.69	0.276	128.29
Representation alignment (proposed)	0.217	86.88	0.256	102.99

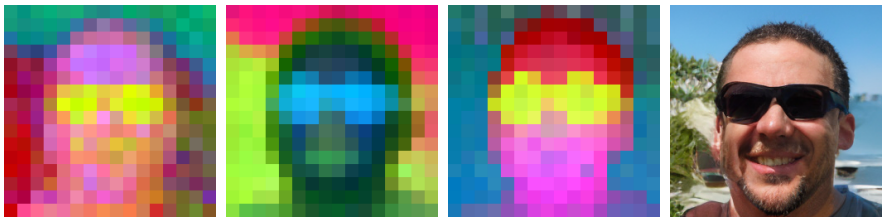


Figure 11: PCA visualizations of patch-level representations. From left to right: representations from a standard diffusion model, representations from a diffusion model trained with REPA, DINOv2 features, and the corresponding input image.

A.14 Representation Alignment on an Independently Pretrained Model

The effectiveness of REPA for inverse problems relies on the availability of a mapping g_ϕ between the internal representations of the diffusion model and the DINOv2 feature space. Such a mapping arises naturally when the diffusion model is pretrained with representation alignment. However, when starting from an independently pretrained diffusion model, this mapping is not readily available. We describe here how to obtain such a mapping in this setting.

A natural approach is to learn g_ϕ from pairs of diffusion and DINOv2 representations extracted from the same images. Specifically, given a dataset $\{x_i\}_{i=1}^{n_0} \subset \mathbb{R}^k, \quad n_0 \in \mathbb{N}$ and a pretrained encoder $f : \mathbb{R}^k \to \mathbb{R}^{N \times D_1}$, we train g_ϕ by maximizing the REPA objective:

$$\mathcal{L}_{\text{REPA}}(\phi) = \mathbb{E}_{x,\, t,\, \epsilon} \left[\frac{1}{N} \sum_{n=1}^{N} \cos\Big(f^{[n]}(x),\, g_\phi^{[n]}(h_t) \Big) \right], \tag{25}$$

where the intermediate diffusion representation is given by $h_t = \text{DIFFENC}(x_t, t) \in \mathbb{R}^{N \times D_2}$. Here, $f^{[n]}(x) \in \mathbb{R}^{D_1}$ denotes the corresponding patch-level representation produced by the DINOv2 encoder. Importantly, only the mapping g_ϕ is optimized, while both the diffusion model (through DIFFENC) and the encoder f remain frozen. As a result, learning g_ϕ is computationally lightweight compared to full diffusion model training.

We consider two parameterizations of g_ϕ. The first follows [42] and applies a token-wise MLP independently to each patch. The second parameterizes g_ϕ as a lightweight Transformer-style network operating on patch-level representations. Given input tokens $h_t \in \mathbb{R}^{N \times D_2}$, the model first applies a linear projection to an intermediate dimension D. The resulting tokens are augmented with learned positional embeddings and processed by a stack of L Transformer encoder blocks. Each block consists of a multi-head self-attention layer followed by a feed-forward network, with residual connections. Finally, a linear projection maps the output tokens to the DINOv2 feature space, yielding $g_\phi(h_t) \in \mathbb{R}^{N \times D_1}$. In our experiments, we use $D = 768$, $L = 2$, and 4 attention heads.

We train the mapping g_ϕ on the FFHQ dataset for 15k iterations using the alignment objective described above. Training is performed with batch size 256 and learning rate 10^{-4} using the AdamW optimizer. We present the resulting alignment curves in for different timesteps in Figure 12. The corresponding training setup is summarized in Table 8. We observe that the token-wise MLP is able to learn a meaningful mapping, but achieves lower alignment compared to both the attention-based parameterization and a model pretrained with representation alignment.

To motivate the need for a more expressive mapping between independently pretrained diffusion representations and the DINOv2 feature space, we visualize PCA feature maps similar to those in [42]. As shown in Figure 11, representations extracted from a standard diffusion model appear significantly noisier and less spatially coherent than those produced by a REPA-pretrained model or DINOv2. The observed structure suggests that recovering semantically aligned features benefits from aggregating information across spatial locations.

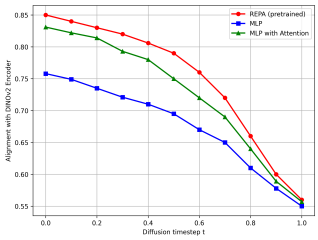


Figure 12: Alignment with the DINOv2 encoder across diffusion timesteps for different parameterizations of g_ϕ. The red curve corresponds to a model pretrained with representation alignment, the blue curve to a token-wise MLP, and the green curve to the attention-based mapping.

Table 8: Comparison of training cost across components.

Model	Trainable parameters	Training steps	Batch size	Optimizer
SiT full model	136.9M	100k	256	AdamW (10^{-4})
MLP mapping g_ϕ	7.3M	15k	256	AdamW (10^{-4})
Attention mapping g_ϕ	15.6M	15k	256	AdamW (10^{-4})

A.15 Results with an Independently Pretrained Model

We apply our inference-time regularizer to inverse problems using the learned mapping. Table 9 reports the corresponding results, alongside those obtained with a model pretrained with representation alignment. Across all inverse problems, incorporating our regularizer consistently improves perceptual metrics (LPIPS and FID), demonstrating that learning the mapping g_ϕ alone is sufficient to enable effective use of REPA at inference time. More specifically, both learned mappings improve over the baseline Latent DPS (SiT), with the attention-based parameterization consistently outperforming the token-wise MLP across all tasks. While the MLP already yields gains, incorporating attention further improves LPIPS and FID. These trends are consistent with our theoretical analysis: performance is governed by the accuracy of the learned mapping, as captured by the $\mathrm{MisREPA}$ error. In this view, the attention-based mapping achieves lower $\mathrm{MisREPA}$, leading to improved alignment and downstream performance, while models pretrained with representation alignment correspond to the smallest mismatch and therefore achieve the strongest overall results.

Table 9: Performance comparison on FFHQ ($\sigma = 0.05$).

Task	**Method**	**LPIPS↓**	**FID↓**	**PSNR↑**	**SSIM↑**
$4\times$ SR	Latent DPS (REPA-backbone)	0.188	56.69	28.99	0.814
	↪ + REPA regularization	**0.176**	**51.27**	**29.12**	**0.819**
	Latent DPS (SiT backbone)	0.190	61.36	28.92	0.805
	↪ + REPA (MLP mapping)	0.184	56.17	28.95	0.809
	↪ + REPA (Attention mapping)	**0.177**	**54.21**	**28.97**	**0.814**
Gaussian Deblur	Latent DPS (REPA-backbone)	0.192	60.65	28.15	0.783
	↪ + REPA regularization	**0.186**	**55.53**	**28.21**	**0.787**
	Latent DPS (SiT backbone)	0.193	60.72	28.02	0.782
	↪ + REPA (MLP mapping)	0.191	58.92	28.09	0.770
	↪ + REPA (Attention mapping)	**0.187**	**58.56**	**28.17**	**0.778**
Motion Deblur	Latent DPS (REPA-backbone)	0.170	52.14	**27.20**	**0.773**
	↪ + REPA regularization	**0.165**	**47.18**	27.16	0.772
	Latent DPS (SiT backbone)	0.171	54.01	**28.02**	**0.779**
	↪ + REPA (MLP mapping)	0.171	52.93	27.73	0.769
	↪ + REPA (Attention mapping)	**0.167**	**49.94**	27.89	0.775

A.16 Additional Qualitative Results

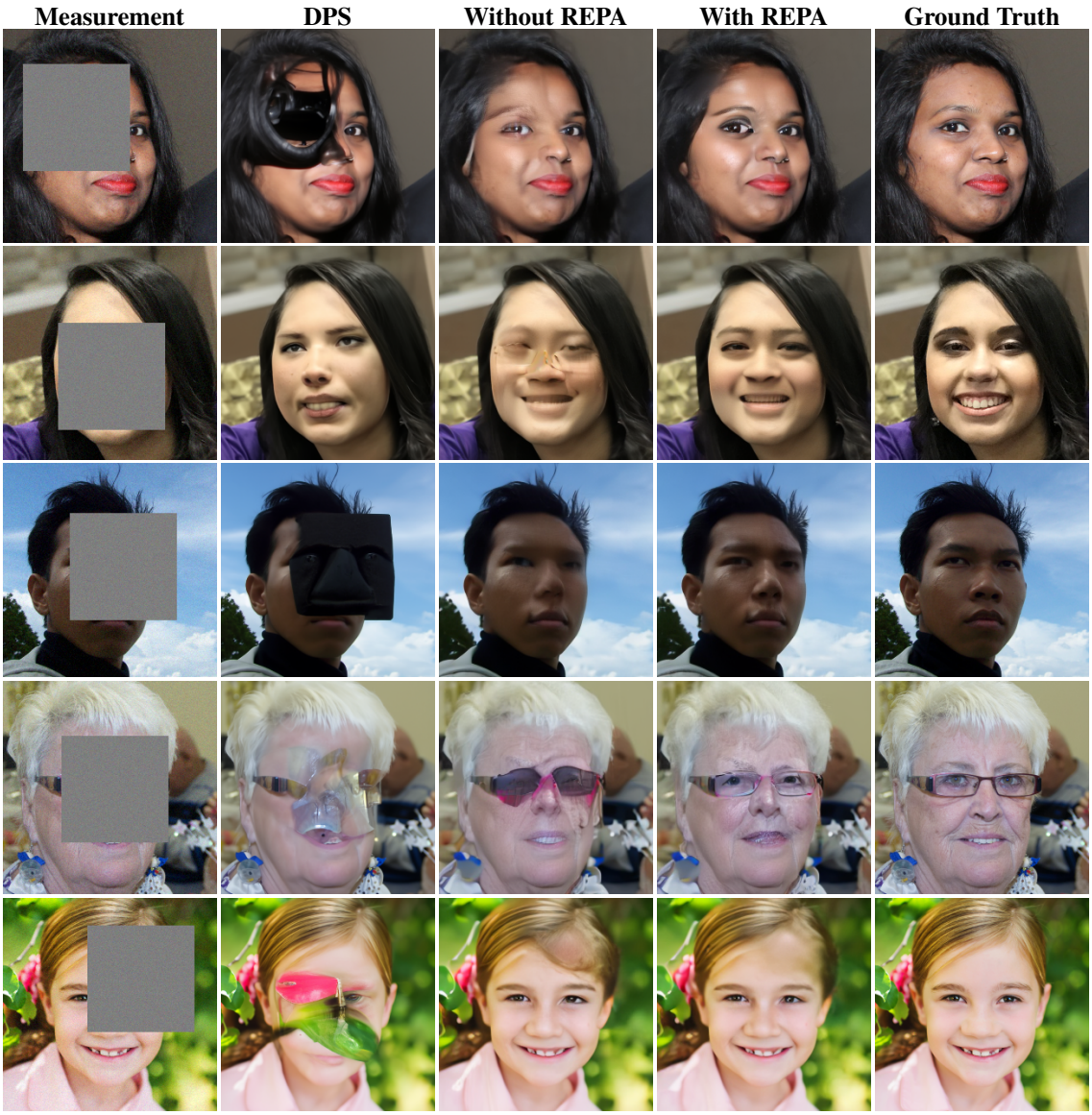


Figure 13: Qualitative comparison for box inpainting on the FFHQ dataset. Each row shows, from left to right: the measurement, DPS, the baseline latent solver, its REPA-enhanced variant, and the ground truth.

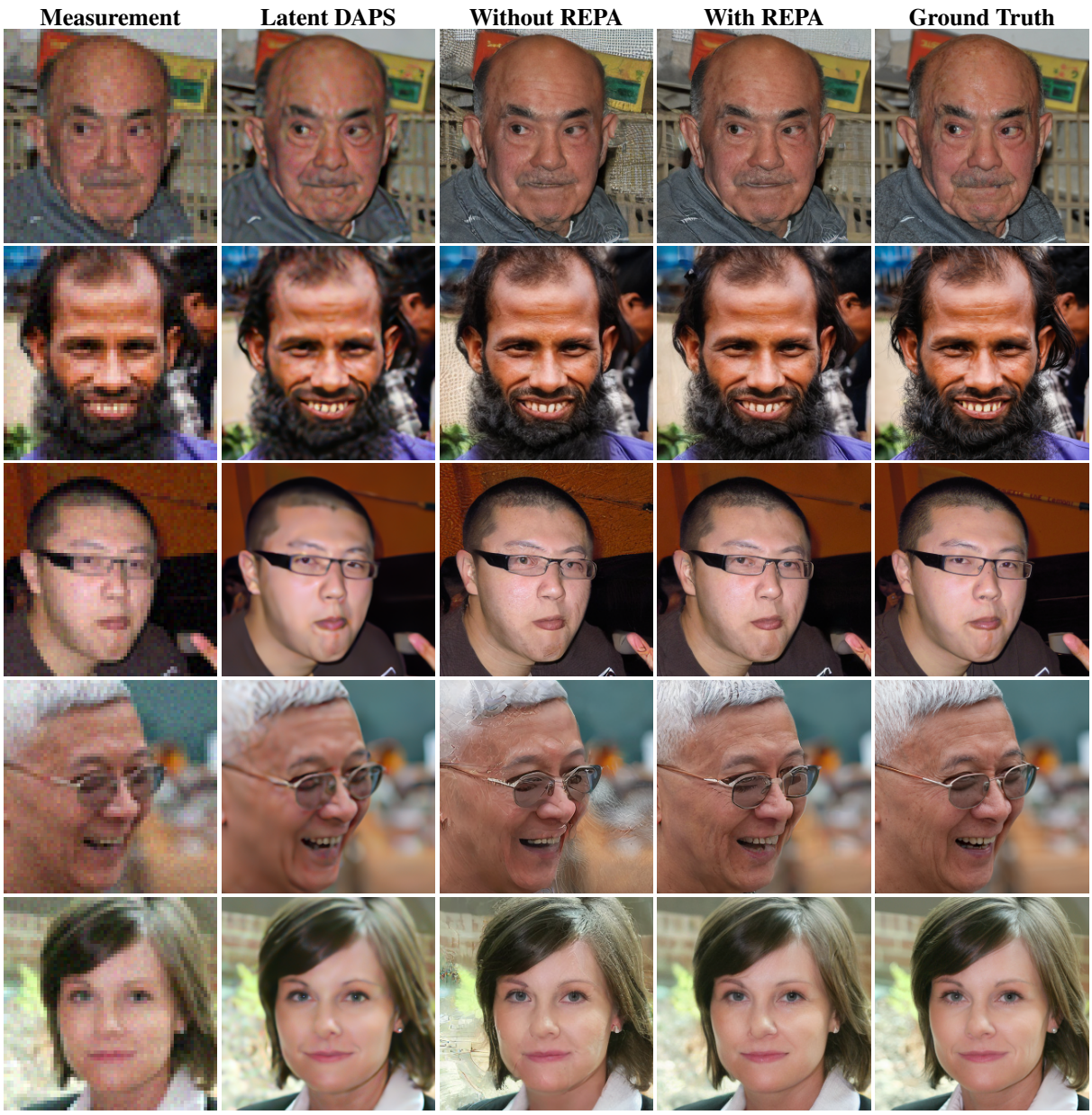


Figure 14: Qualitative comparison for $4\times$ super-resolution on the FFHQ dataset. Each row shows (from left to right): the measurement, the baseline method (Latent DAPS), the baseline latent solver (Latent DPS or ReSample), its REPA-enhanced variant, and the ground truth. The first two rows correspond to ReSample, while the last three correspond to Latent DPS.

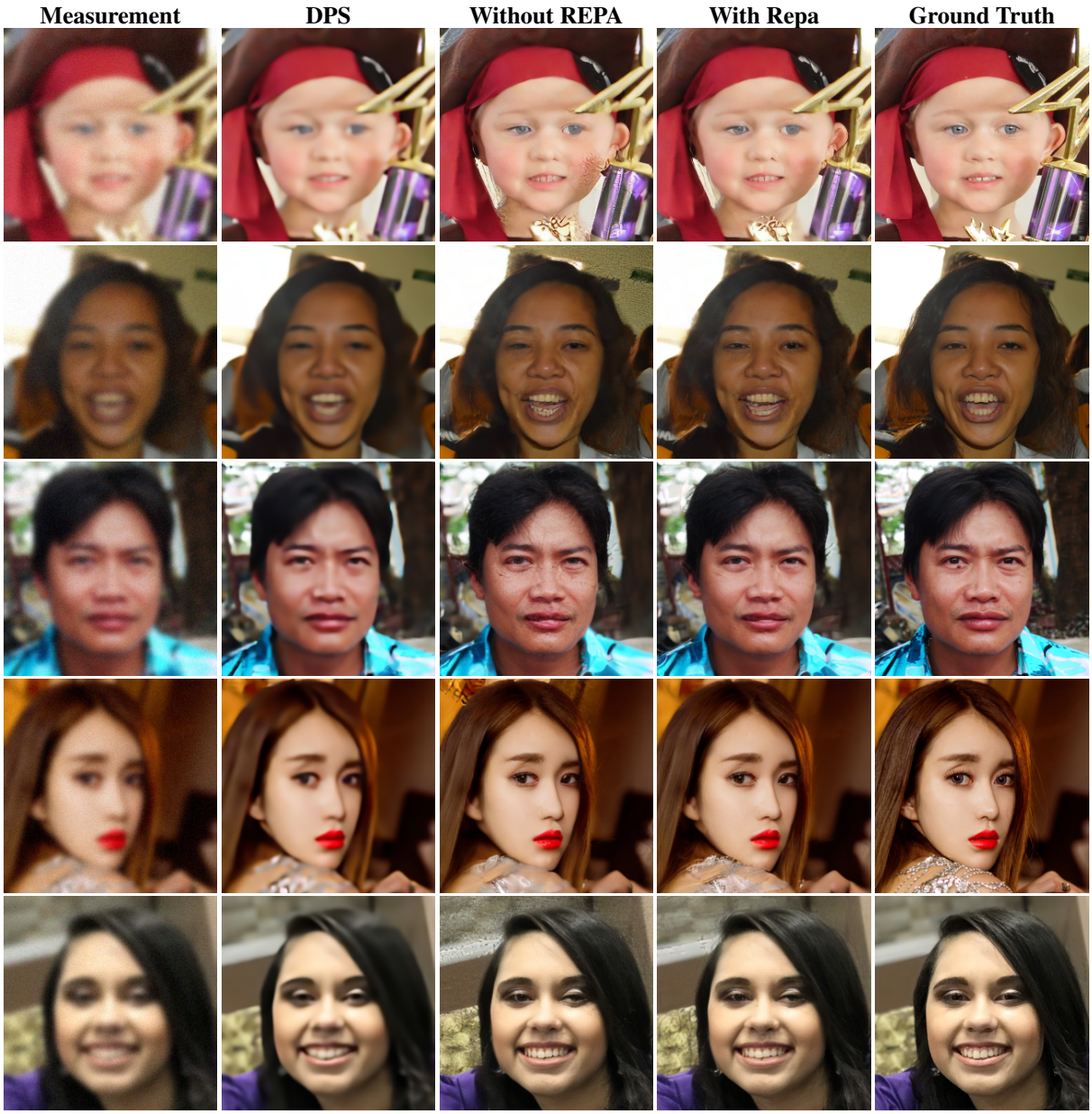


Figure 15: Qualitative comparison for Gaussian Deblurring on the FFHQ dataset. Each row shows (from left to right): the measurement, the baseline method (Latent DAPS), the baseline latent solver (Latent DPS or ReSample), its REPA-enhanced variant, and the ground truth. The first two rows correspond to ReSample, while the last three correspond to Latent DPS.



Figure 16: Qualitative comparison for Motion Deblurring on the FFHQ dataset. Each row shows (from left to right): the measurement, the baseline method (DPS), the baseline latent solver (Latent DPS or ReSample), its REPA-enhanced variant, and the ground truth. The first two rows correspond to ReSample, while the last three correspond to Latent DPS.



Figure 17: Qualitative comparison for box inpainting on the ImageNet dataset. Each row shows (from left to right): the measurement, the baseline method (DPS), the baseline latent solver (Latent DPS or ReSample), its REPA-enhanced variant, and the ground truth. The first three rows correspond to ReSample, while the last two correspond to Latent DPS.

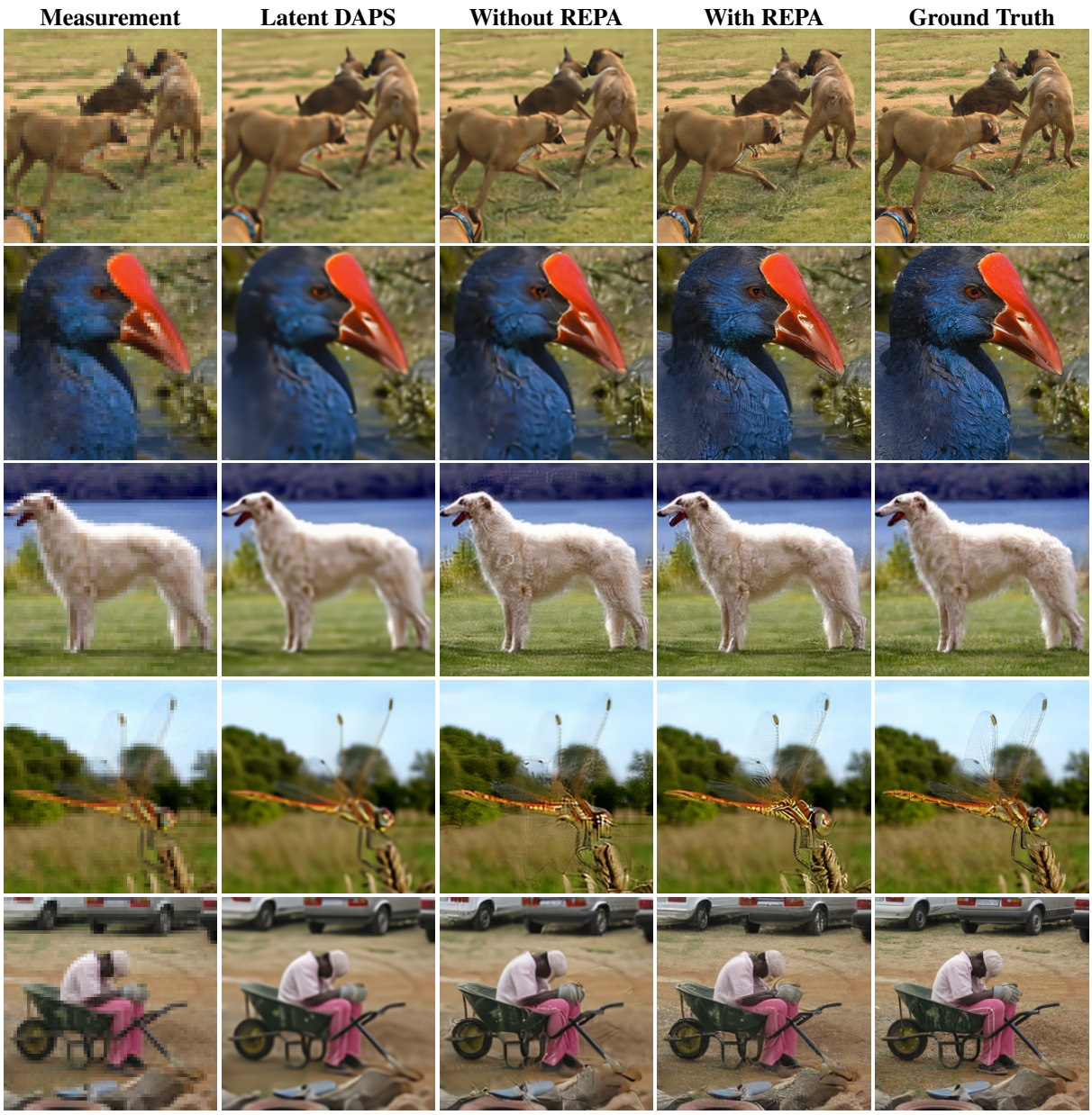


Figure 18: Qualitative comparison for Super resolution on the ImageNet dataset. Each row shows (from left to right): the measurement, the baseline method (Latent DAPS), the baseline latent solver (Latent DPS or ReSample), its REPA-enhanced variant, and the ground truth. The first three rows correspond to ReSample, while the last two correspond to Latent DPS.

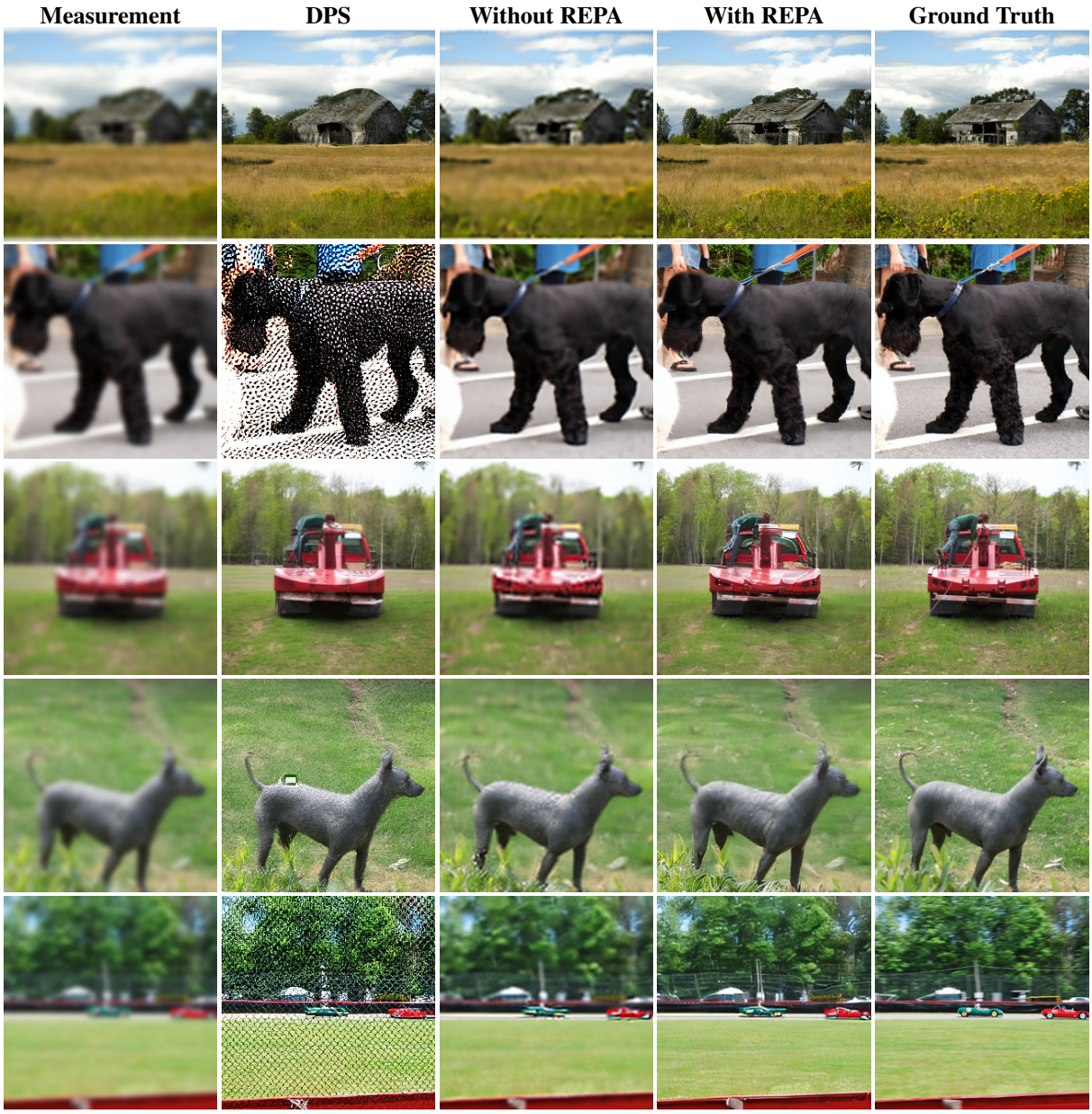


Figure 19: Qualitative comparison for Gaussian Deblurring on the ImageNet dataset. Each row shows (from left to right): the measurement, the baseline method (DPS), the baseline latent solver (Latent DPS or ReSample), its REPA-enhanced variant, and the ground truth. The first three rows correspond to ReSample, while the last two correspond to Latent DPS.

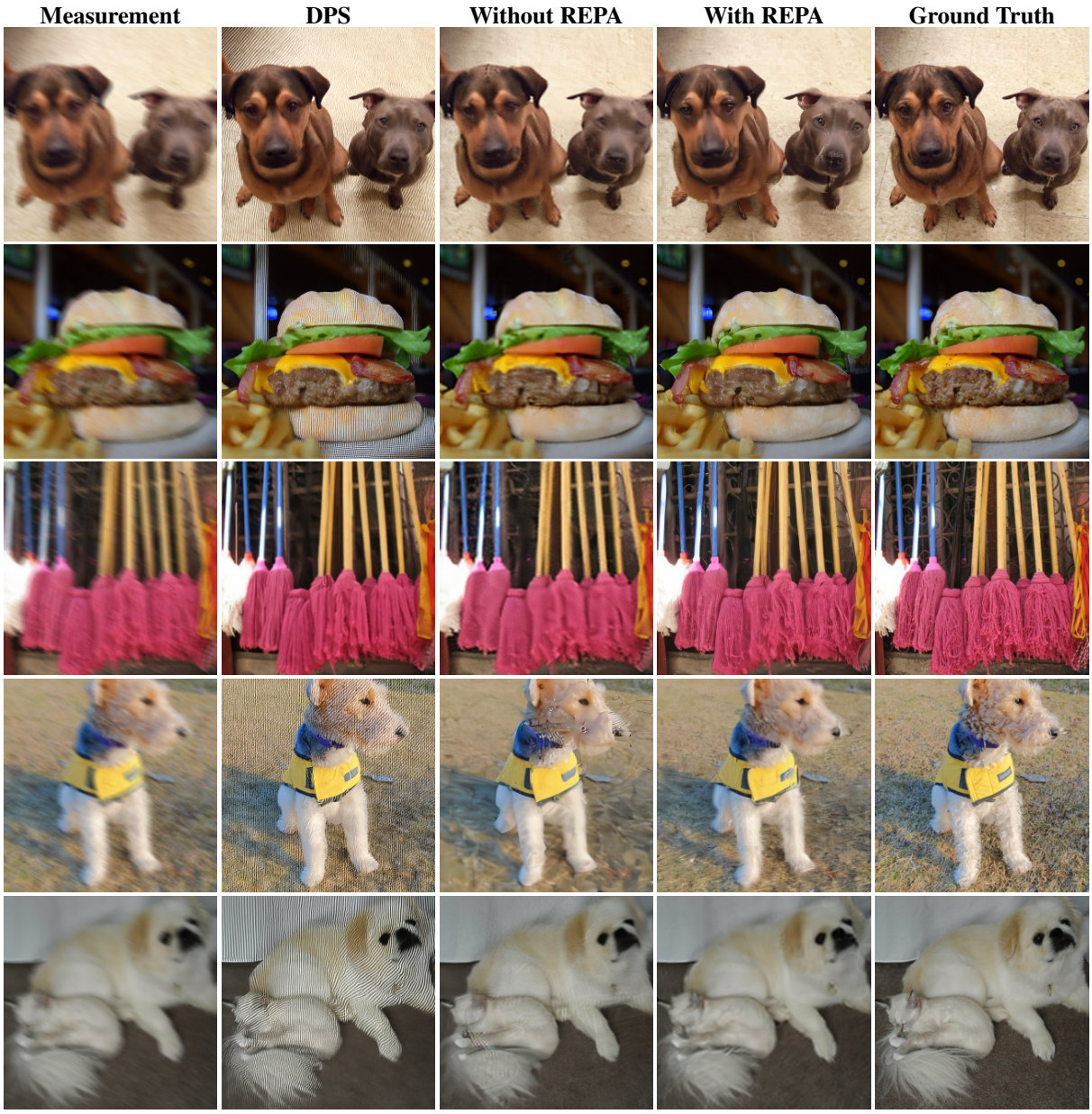


Figure 20: Qualitative comparison for Motion Deblurring on the ImageNet dataset. Each row shows (from left to right): the measurement, the baseline method (DPS), the baseline latent solver (Latent DPS or ReSample), its REPA-enhanced variant, and the ground truth. The first three rows correspond to ReSample, while the last two correspond to Latent DPS.